Supporting Information for

Covalent Organic Framework with Electrodeposited Copper Nanoparticles- a Desirable Catalyst for Ullmann Coupling Reaction

Chandana Chandran,[a]¥ Himan Dev Singh,[a]¥ Liya S Leo,[a] Pragalbh Shekhar,[a] Deepak Rase,[a] Debanjan Chakraborty,[a] Chathakudath P. Vinod[c] and Ramanathan Vaidhyanathan*[a][b]

[a] Department of Chemistry, Indian Institute of Science Education and Research, Dr. Homi Bhabha Rd. Pashan, Pune, 411008. E-mail: vaidhya@iiserpune.ac.in (R.V.).

[b] Centre for Energy Science, Indian Institute of Science Education and Research, Dr. Homi Bhabha Rd. Pashan, Pune, 411008. E-mail: vaidhya@iiserpune.ac.in (R.V.).

[c] Catalysis Division, CSIR-National Chemical Laboratory, Dr. Homi Bhabha Rd. Pashan, Pune, 411008.

¥ These authors contributed equally

List of contents

---

1. Materials and Methods

All the chemicals like phenylenediamine, copper sulfate pentahydrate, copper acetate monohydrate, potassium carbonate, iodobenzene, phenol and its derivatives are used without purification after having been purchased from Sigma Aldrich. 2,4,6-triformylresorcinol was synthesized using previously reported procedure. Solvents used were ethanol, distilled water, DMF, ethyl acetate, hexane.

Synthesis of 2,4,6-Triformylresorcinol:

2,4,6-Triformylresorcinol was synthesized used a reported procedure.[S1] 65 mmol of resorcinol (7.16 g) was dissolved in 70 mL of trifluoroacetic acid and 20 g of hexamine was added to it. The mixture was refluxed at 120°C for 24 hrs under N_2 atmosphere. The contents were further heated at 150°C for 3 hrs and cooled back to 120°C. About 110 mL of 3 N HCl was added to it and heated at 105°C for 30 minutes. This yielded a dark yellow precipitate, which was filtered off under hot condition.

Larger Scale Synthesis of IISERP-COF15:

IISERP-COF15 was synthesized via the solvothermal method on a larger scale in an autoclave. 360 mg (1.8 mmol) of 2,4,6-triformylresorcinol and 300 mg (2.7 mmol) of phenylenediamine were dissolved in a 50 mL mesitylene and 50 mL dioxane solvent mixture. Contents were stirred at room temperature for 4 hrs. Then 5 mL of 6 N acetic acid was added and stirred for another 30 minutes. Then the mixture was frozen in liq. N_2 and kept in the oven for 3 days at 120°C. (Scheme S1) The product was a dark brown precipitate that was washed with methanol. Obtained a yield of 92 % with formula $C_{36}N_6O_4H_{24}$ and molecular weight 604.62 $gmol^{-1}$.

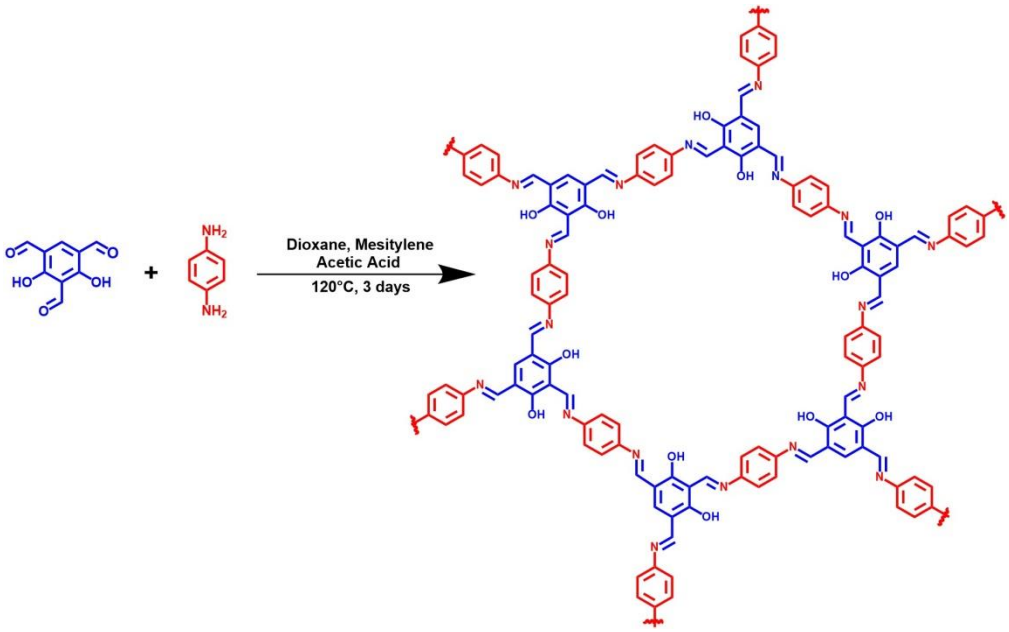

Scheme S1. Schematic representation of IISERP-COF15 synthesis.

Synthesis of Cu@COF via Electrochemical Deposition:

About 50 mg of IISERP-COF15 was dispersed in 3 mL ethanol and 50 μL nafion binder and was ground thoroughly for 30 minutes. The slurry was then coated on Platinum (Pt) gauze and kept for drying overnight. The electrolyte was prepared by dissolving copper acetate monohydrate in ethanol-water mixture. The ratio of ethanol to water was 1:3 and it was dissolved to get a light blue colored solution. To this, 15 mL of 1 M H_2SO_4 was added and this solution was used as the electrolyte. This was subjected to Cyclic Voltammetry (CV) in a large electrochemical cell. COF coated on Pt gauze was used as the working electrode, the Ag/AgCl as the reference and the Pt (larger surface area intertwined Pt wires) as the counter. CV was run for 800 cycles at a scan rate of 0.1 V/s in the potential range -0.3 V to 0.6 V. After the completion of CV, the COF powder was removed from the platinum gauze by soaking in ethanol.

Cu@COF formed using varying CV scan rates: After optimizing the electrolyte concentration, the catalyst was also prepared at different CV scan rates. We observed that scan rate significantly affects the size of the Cu nanoparticles. With the increase in the scan rate from 0.025 V/s to 0.1 V/s, the peak corresponding to copper (111) reflection at $2\theta = 43°$ in the PXRD pattern showed a systematic change in intensity (Figure S1). The intensity of this reflection gradually decreases with the increasing scan rate. This intensity change has been co-related to the size of Cu nPs. The deposition of nanoparticles consists of two main processes. The first step is fast nucleation which would be followed up by growth. During the fast scan, the deposition of nPs gets less time, and hence the chances of the formation of bigger nPs via an Ostwald ripening type process are low.

On the other hand, if the deposition time is increased by decreasing the scan rate, the situation favors the growth of larger particles. Since these nanoparticles grown are large, most of these

reside on the surface of the COF and get exposed to the incident X-rays giving rise to intense peaks corresponding to the Cu. In contrast, the smaller nanoparticles grown using fast scan rates are likely to reside in the COF pockets grown to restricted sizes, contributing less reflection intensity. *Note: The trend in the catalytic activity of the Cu@COF prepared under different CV scan rates has been discussed in the main text.*

2. Analytical characterization

Powder X-ray diffraction:

Powder X-Ray has been carried out using a Bruker instrument with a Cu Kα (λ = 1.54 Å) source and processed using PDXL software.

Thermo gravimetric Analysis:

NETSZCH TGA-DSC instrument has been used for TGA analysis. The sample was heated under N_2 flow of 20 mL/min (purge + protective) from 25°C to 600°C with a heating rate of 5 K/min.

Infra-Red spectroscopy (IR):

IR spectra were obtained using a Nicolet ID5 attenuated total reflectance IR spectrometer in a range of 4000-600 cm^{-1}. KBr pellets were made with the sample to record IR.

Nuclear Magnetic Resonance spectroscopy (NMR):

NMR spectra for the catalytic products were recorded on a 400 MHz Jeol ECS-400, Bruker 400 MHz.

Field Emission-SEM:

Ultra Plus Field Emission Scanning Electron Microscope with integral charge compensator and embedded EsB and AsB detectors was used for recording the SEM images and EDX analysis. During sample preparation, the solid samples were dispersed in THF and sonicated for 10 mins. The dispersed samples were drop casted on silicon wafer and dried in a vacuum oven for overnight.

HR-Transmission electron microscopy (HRTEM):

FEI (Jeol FEG 2100F is the model) high-resolution transmission electron microscope (HRTEM) equipped with a field emission source operating at 300 KeV was used for collecting the TEM images. The well dispersed sample was drop casted on a Cu grid.

Adsorption studies:

All the adsorptions were performed using a 3-FLEX pore and surface area analyzer and few cases using Micromeritics ASAP 2020.

Cyclic Voltammetry (CV):

Cyclic Voltammetry studies were performed using an AMETEK instrument and the data was analyzed with Versa Studio software. A typical three electrode assembly was employed, where

Ag/AgCl and Pt wire were used as the reference and the counter electrodes. The working electrode was COF coated on platinum gauze.

Spectro-electrochemistry:

Inside the UV cuvette, a typical three-electrode setup (Pt mesh as working electrode, Ag/AgCl as reference electrode and Pt wire as counter electrode) was built and connected to the Ocean Optics instrument to observe the change of the spectra in situ. 3 mL of 9 mM copper acetate solution (details discussed later) was dispensed into a cuvette and the absorbance was monitored via in-situ UV-Vis spectroscopy under applied potential with the help of a charge-discharge analyzer (CHI760, CH Instruments Inc).

X-ray Photoelectron Spectroscopy:

The XPS and depth profile analysis was carried out using Thermoscientific Kalpha+ spectrometer fitted with monochromatic Aluminum Kα x-ray source (1486.6 eV). The charge neutralization gun was always switched on during the data collection. The spot size of the x-ray was 400 microns. Depth profile analysis was carried out with Argon sputter source at 1000 eV ion energy.

Confocal Microscopy:

Imaging performed on Carl Zeiss LSM 710 microscope. Images were taken at a 10x magnification with excitation from an Ar laser at wavelength of 405 nm and emission was recorded at a wavelength range of 419 nm – 720 nm by PMT.

Stereo Fluorescence Microscopy:

Fluorescent images were collected using Blue GFP fluorescent filter. The excitation was recorded at a wavelength of 379 – 405 nm and the emission at 435 – 485 nm.

3. General procedure for catalytic reaction

In a 25 mL round bottom flask containing 0.25 mol% of Cu@COF, 1 mmol of iodobenzene, 1.2 mmol of phenol and 2.3 mmol of K_2CO_3 was added. To this 6 mL DMF was added and the reaction mixture was kept for reflux under N_2 atmosphere at 135°C for 24 hrs. After this, 10 mL ethyl acetate was added and the catalyst was separated by filtration. The progress of the reaction was monitored using TLC. Then the reaction mixture was extracted using ethyl acetate and washed with brine solution. Then the organic phase was dried with anhydrous Na_2SO_4 and the solvent was evaporated. The crude product was purified using column chromatography. The product was characterized using ^{1}H, ^{13}C Nuclear Magnetic Resonance Spectroscopy and HRMS.

4. Characterizations of COF

A solvothermal reaction was performed on a bulk scale in which phenylenediamine was reacted with triformylresorcinol in mesitylene, dioxane in presence of acetic acid at 120°C for 3 days in a teflon liner. The product was obtained as brown powder by vacuum filtration and it was washed with an excess of DMF, THF and methanol. The crystalline nature of the COF was confirmed by Powder X-ray diffraction (Fig. S1).

Thermogravimetric analysis (TGA) shows that IISERP-COF15 has very good thermal stability upto 380°C (Fig. S2). COF shows 39 % mass loss upto 244°C in two steps which can be attributed to the solvents residing on the COF surface and solvent molecules occluded in the nanopores. Such large solvent content is typically attributable to microporous structure, and this is consistent with the fact that our COF is built from relatively smaller tripodal monomers. The Infra-Red (IR) stretching band at 1609 cm^{-1} is assigned to the vibration of C=O bonds, peaks at 1517 and 1454 cm^{-1} are observed corresponding to the stretching vibrations of C=N and C=C-N bonds, respectively (Fig. S3). Porosity investigation was done for the as made COF and the permanent porosity was established by N_2 adsorption isotherm at 77 K. It shows a type-I isotherm with a saturation uptake of 16 mmol/g (Fig. S4). BET and Langmuir surface areas were estimated using the adsorption branch of nitrogen isotherm and it has come out to be 1369 and 1739 m^2/g, respectively, which is slightly on the higher side than the previously reported by Chakraborty et al (Fig. S5). (S1) NLDFT fit to the adsorption branch of N_2 isotherm shows that COF is microporous and it has a major pore size of 1.3nm (Fig. S7). Microscopic studies were performed to observe the morphology of the COF, FESEM shows that COF has snow grain like morphology, these small grains have aggregated together to give flakes, stacked over each other, like appearance (Fig. S8A-B). From

HRTEM, lattice planes can be observed which reflect the highly crystalline nature of IISERP-COF15, HRTEM shows that COF consists of flakes which are overlapped on each other, as observed from FESEM (Fig. S9 A-C).

Powder X-Ray Diffraction:

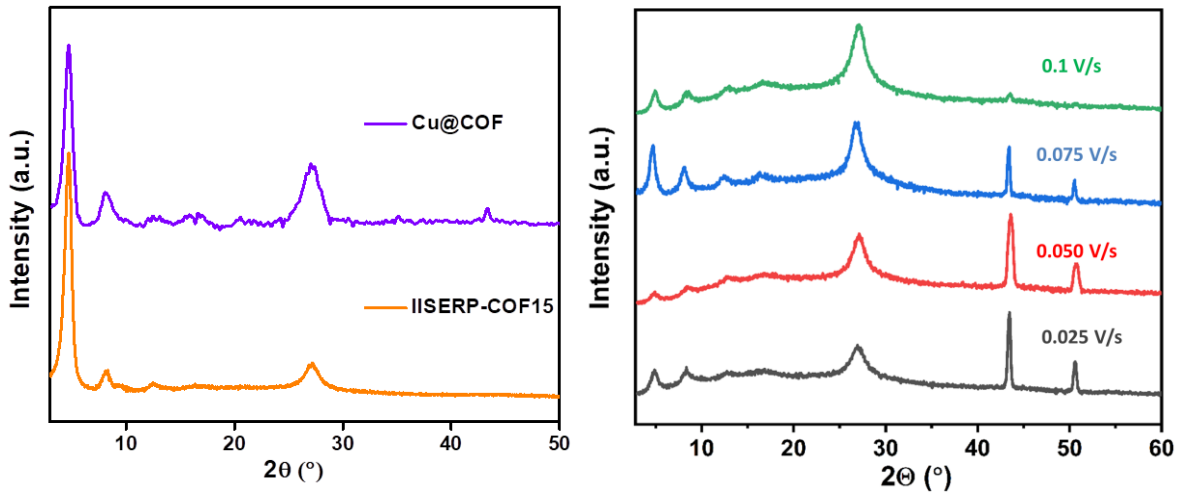

Figure S1. Left: PXRD pattern of IISERP-COF15 and Cu@COF. The increase in the relative intensity of the (001) reflection ($2\theta = 28^{o}$) has contributions from slightly lowered crystallinity and potential exfoliation of the COF under the wet electrochemical conditions. Right: PXRD of Cu@COF synthesized at different CV scan rates.

Thermo Gravimetric Analysis:

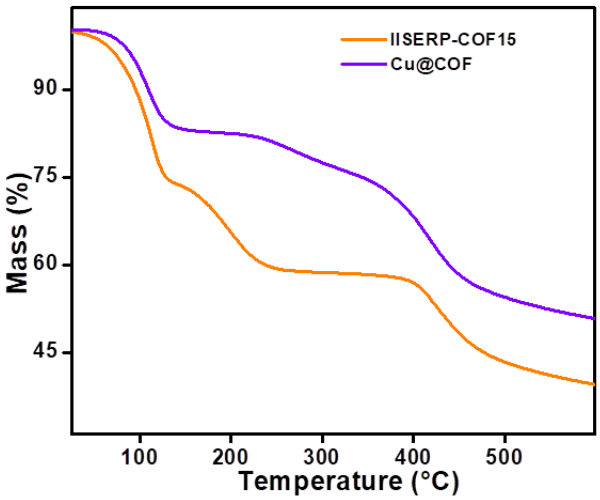

Figure S2. TGA profile of IISERP-COF15 and Cu@COF.

Notes from TGA: As synthesized IISERP-COF15: The large weight loss in the temperature range of 25-250°C is due to the loss of the high-boiling solvents (dioxane and mesitylene) from

the pores. Such high solvent accessible spaces aptly justifies the microporous structure of the COF. The COF shows exceptional thermal stability up to 380°C.

Cu@COF: Significant solvent loss from the Cu@COF sample in a similar temperature window confirms the ample porosity retained even after the nanoparticle loading. This also justifies the nanoparticles being small and hence do not block the pores. However, the noticeable lowered total weight loss for the Cu@COF reveals the copper loading (3.25 %, this agrees well with the Cu loading estimated from the EDX analysis).

Infra-red spectroscopy:

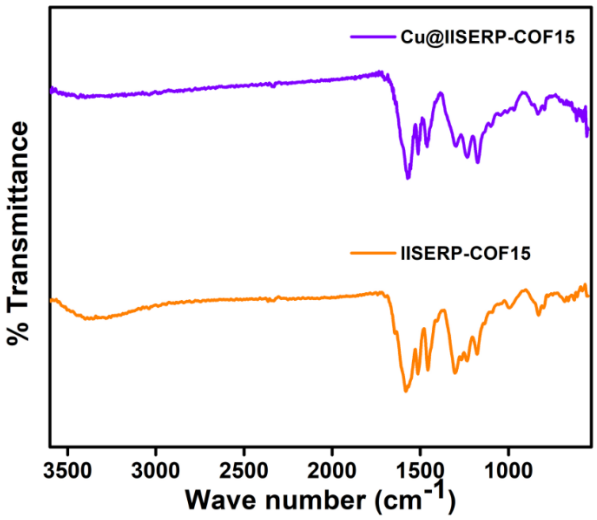

Figure S3. Comparison of the IR spectra of IISERP-COF15 and Cu@ COF. The peaks corresponding to the COF framework are intact in the copper loaded sample.

Adsorption studies:

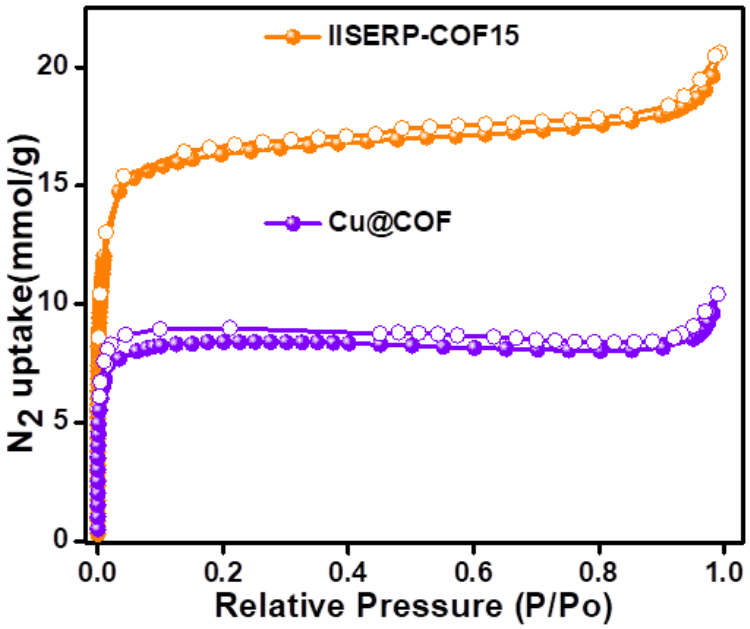

Figure S4. Nitrogen adsorption isotherm of IISERP-COF15 and Cu@COF measured at 77K. Type I isotherm suggestive of microporous structure is seen.

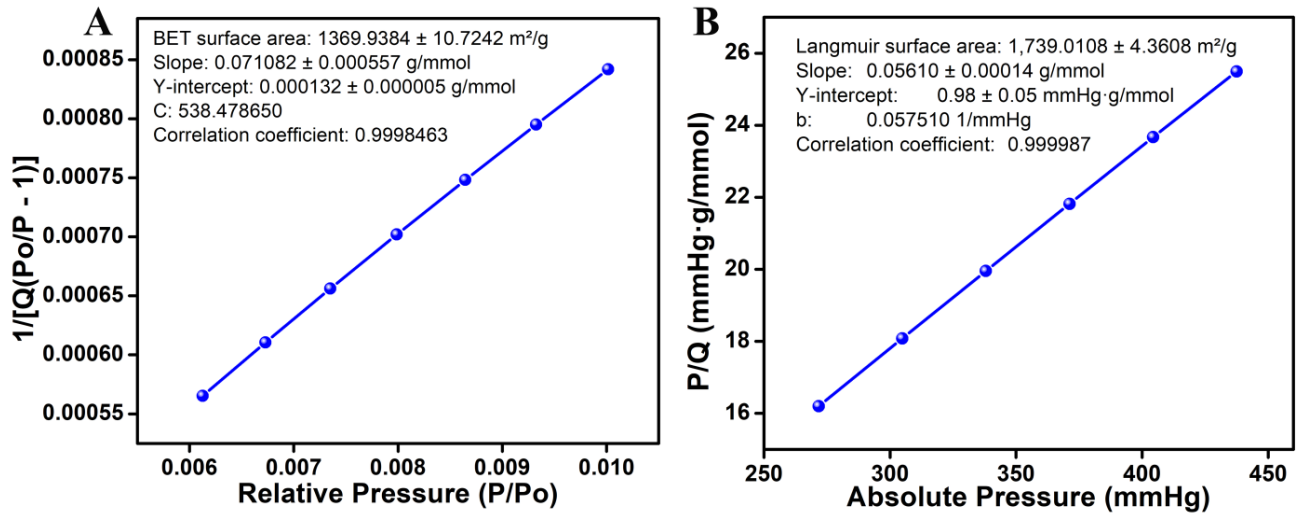

Figure S5. (A) Brunauer–Emmett–Teller surface area plot for IISERP-COF15. (B) Langmuir surface area plot for IISERP-COF15.

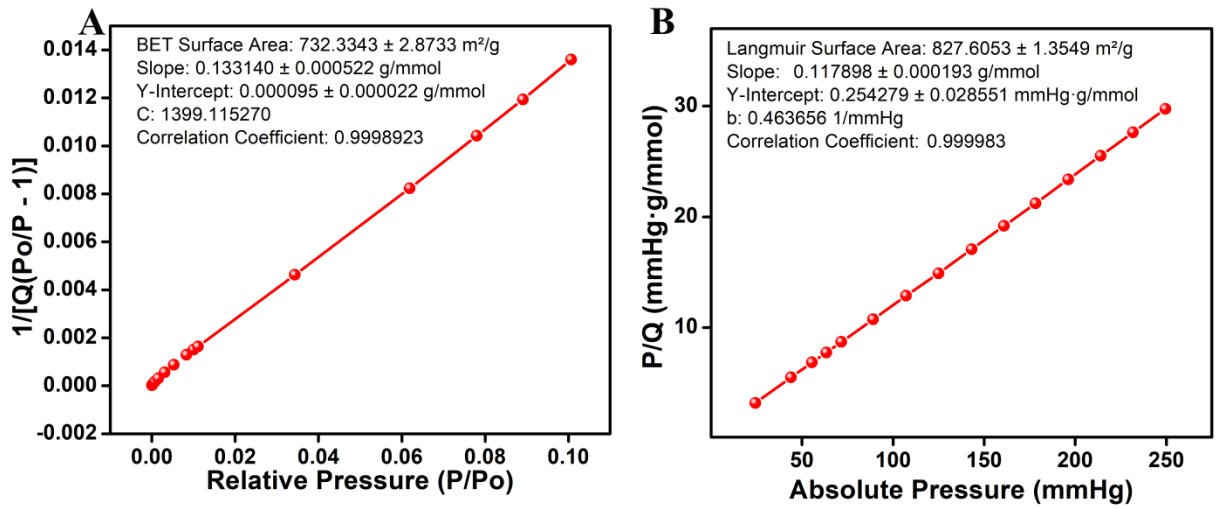

Figure S6. (A) Brunauer–Emmett–Teller surface area plot for Cu@COF. (B) Langmuir surface area plot for Cu@COF.

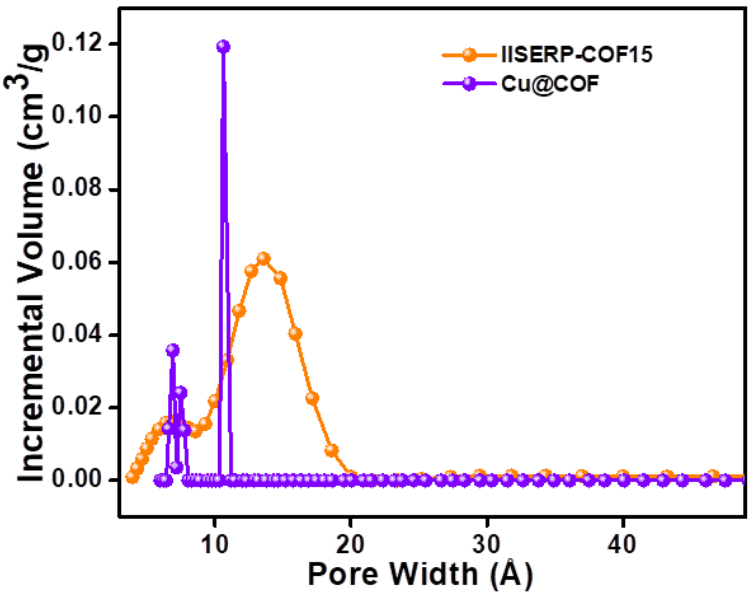

Figure S7. Shows the pore size distribution of IISERP-COF15 and Cu@COF. The narrower pore-size distribution in the Cu@COF is seen.

Microscopic Studies:

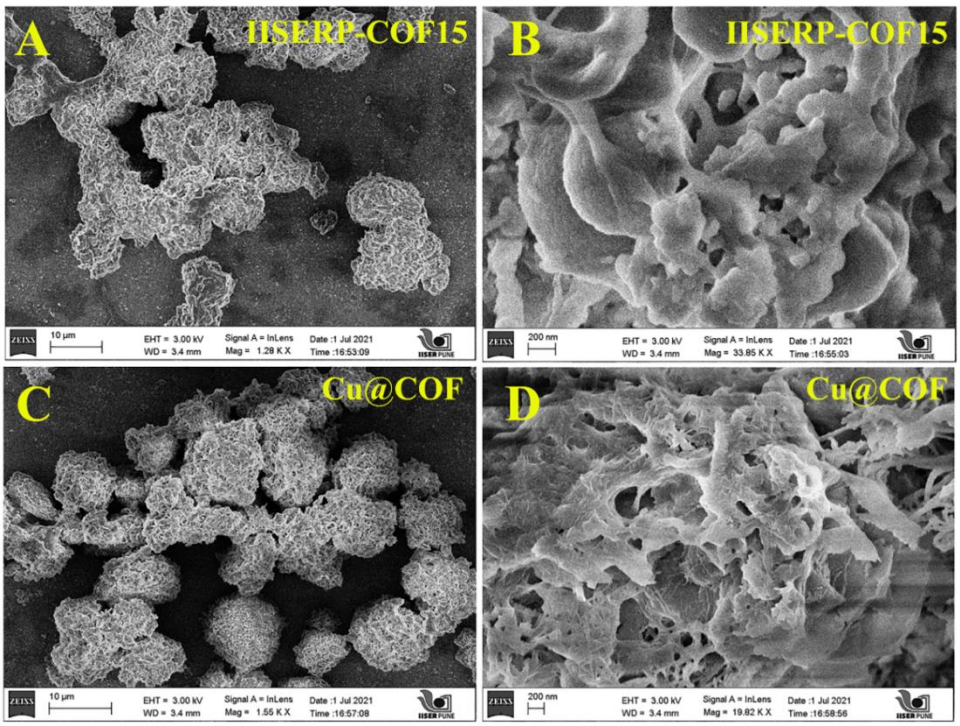

Figure S8. (A, B) Scanning Electron Microscopic images of IISERP-COF15. (C,D) Scanning Electron Microscopic images of Cu@COF.

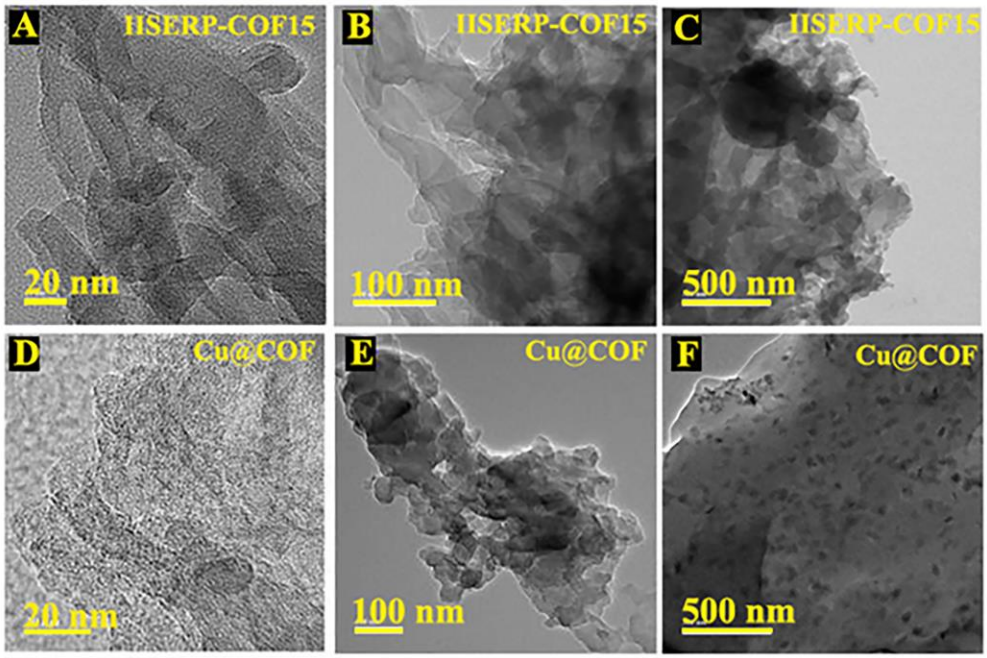

Figure S9. (A,B,C) HRTEM images of IISERP-COF15 at different magnifications. (D,E,F) HRTEM images of Cu@COF at different magnifications.

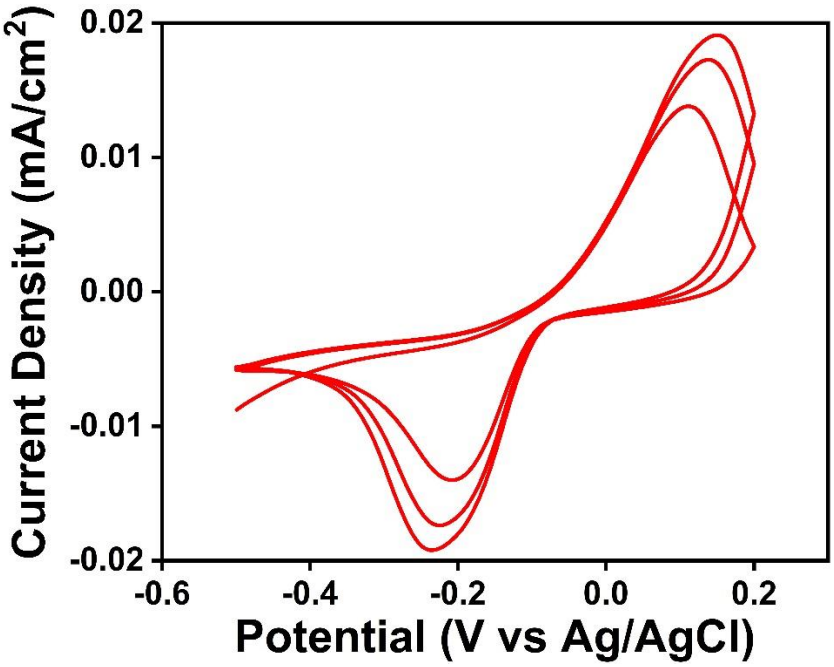

Figure S10. Cyclic voltammogram recorded in an in-situ spectro-electrochemical measurement recorded during the loading of copper nPs into the COF.

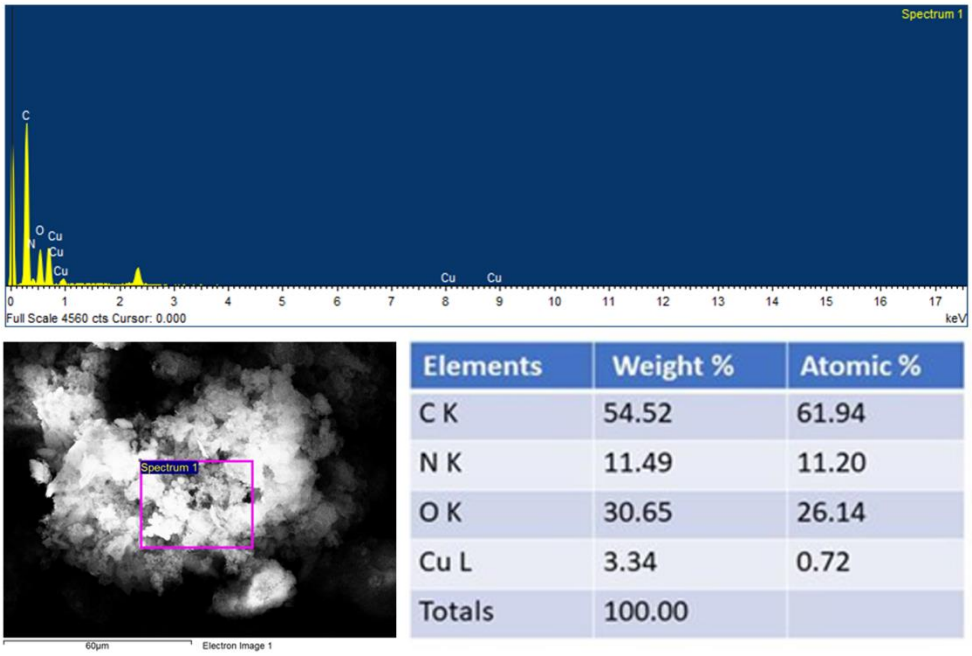

Elements	Weight %	Atomic %
C K	54.52	61.94
N K	11.49	11.20
O K	30.65	26.14
Cu L	3.34	0.72
Totals	100.00	

Figure S11. Energy Dispersive X-Ray (EDX) images of Cu@COF.

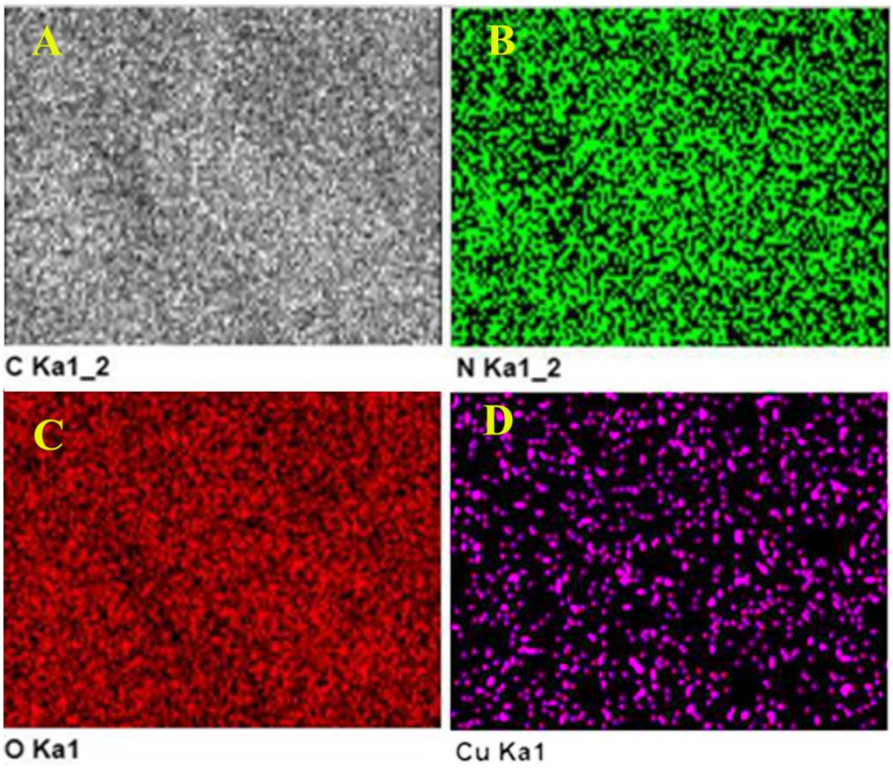

Figure S12. Elemental mapping of Cu@COF.

5. Characterizations of the spent catalyst (spent Cu@COF)

Microscopic Studies:

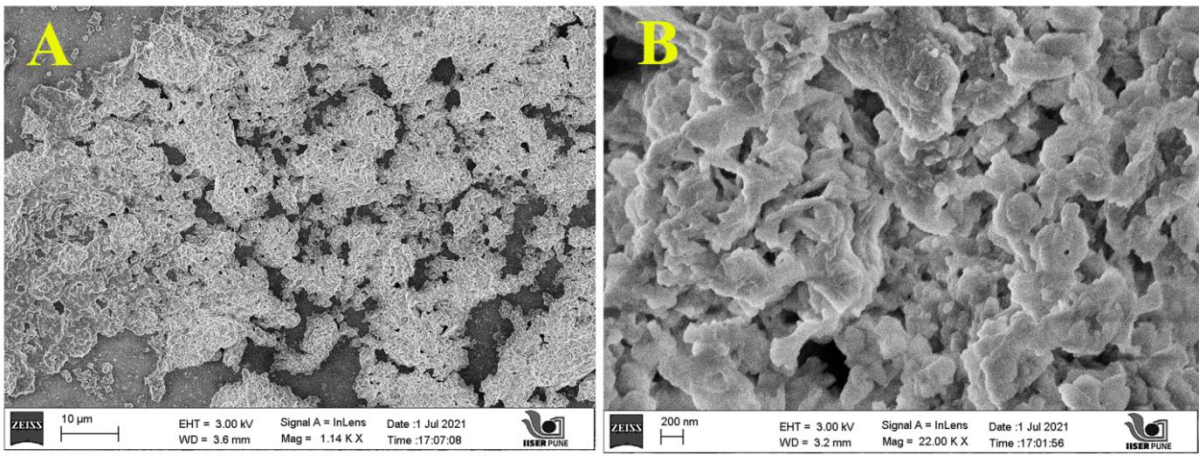

Figure S13. FESEM images of Cu@COF after catalysis.

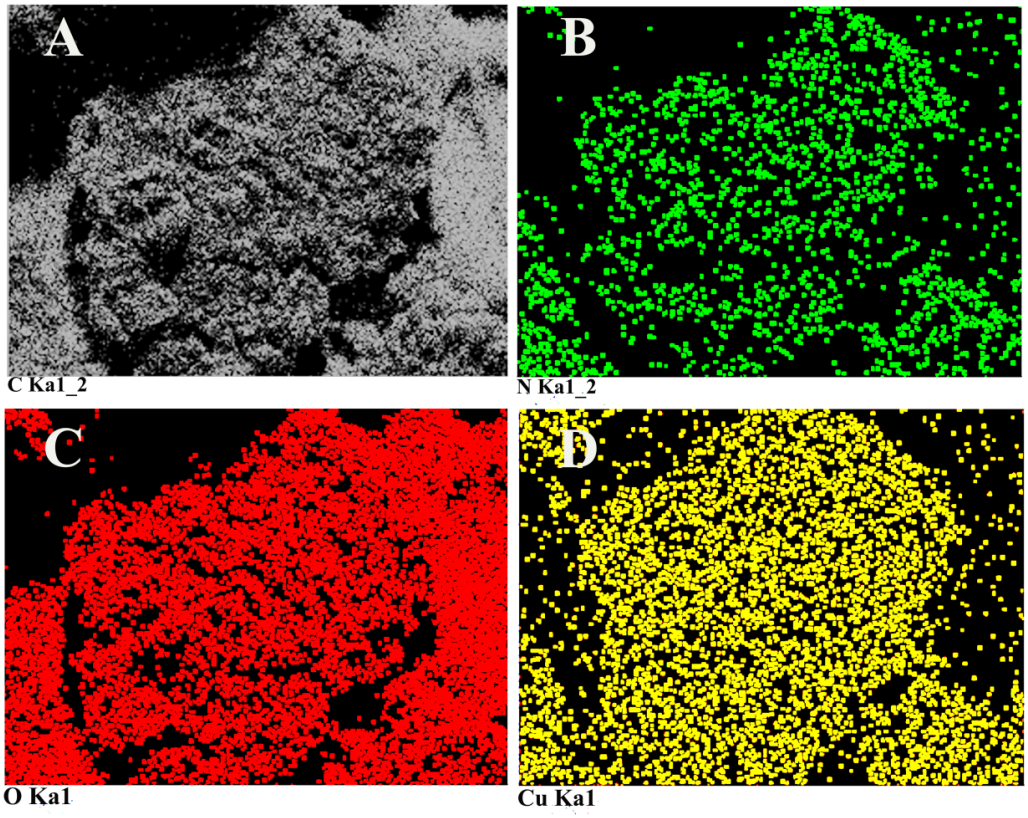

Figure S14. Elemental mapping of Cu@COF after catalysis.

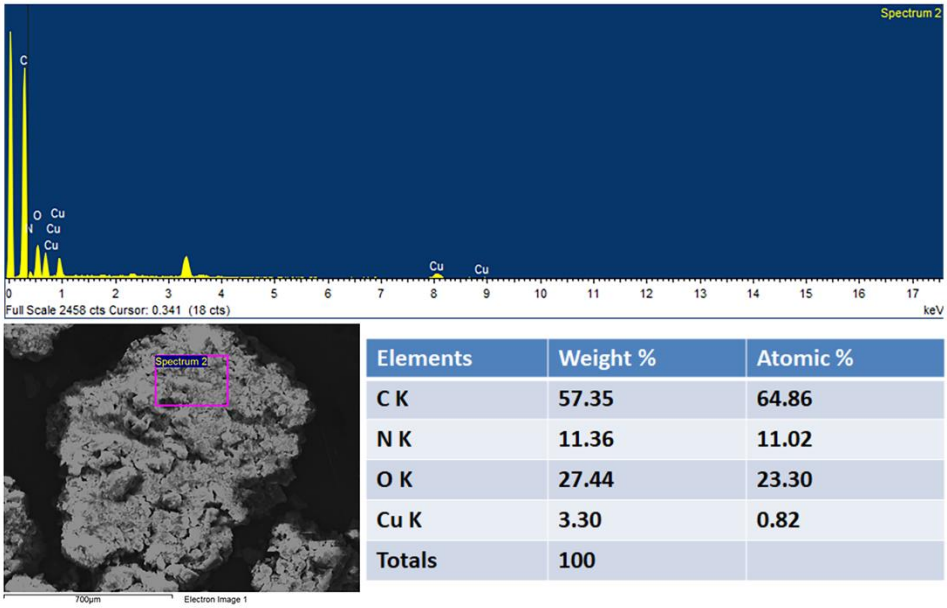

Elements	Weight %	Atomic %
C K	57.35	64.86
N K	11.36	11.02
O K	27.44	23.30
Cu K	3.30	0.82
Totals	100	

Figure S15. Energy dispersive X-Ray (EDX) images of Cu@COF after catalysis.

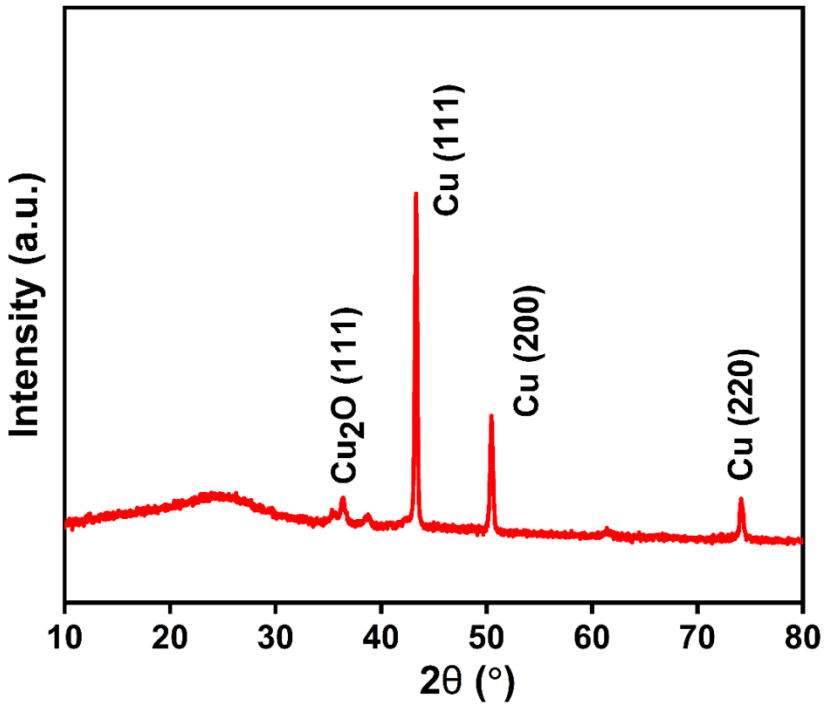

Figure S16. PXRD of pyrolysed Cu@COF after catalysis depicting no change in the oxidation state of nanoparticles.

6. Computational Modeling Details

The crystallographic modeling of the structure of the COF and its DFT optimization have been reported elsewhere.[S2] The structure of the Cu@COF was arrived at using the Monte-Carlo-based Simulated Annealing algorithm embedded in the Materials Studio V.8 (Accelrys).[S3-S5] For the structure optimization, Automatic temperature control over 100000 cycles/cell was employed. Universal force filed (UFF) in conjugation with a QEq charge equilibration method was used for the geometry optimization. No constraints were placed. The optimized structure of the Cu@COF had relative energy higher than the empty COF (Cu@COF = -91.82(2) kcal/mol/uc; COF = -78.17(1) kcal/mol/uc), which is expected.

To calculate the frontier orbitals, we used the DMOL^3 module[S6] with a high tolerance of $1x10^{-8}$ for the SCF convergence and a global cut-off of 4.4 Å. UFF-based Lennard-Jones dispersion corrections were included in Energy, Force and Displacement calculations. All calculations are at 0K and were spin-unrestricted, adopting the formal spin as the initial spin. A Smearing parameter of 0.02 Ha was applied.

Core elements were treated with all-electron pseudopotentials and the DNP basis set. The dispersion corrected DFT calculations employed a plane wave basis cut-off of 500 eV. For our dispersion corrected DFT optimizations, we used Generalized Gradient Approximation (GGA) for calculating the exchange and the correlation energies and employed the Perdew-Wang 91 (PW91) functional. Density mixing was done using the Pulay scheme. The adsorption energies were estimated from a large 6 x 6 x 6 COF matrix embedded with the copper clusters, wherein the substrate molecules were made to find their optimized positions via a Simulated annealing routine. The Monte Carlo step sizes were automatically adjusted during this process. We used the smart algorithm with an ultra-fine convergence tolerance. We employed 100000 loading steps with 10 heating cycles having 10000 steps per cycle. The Lennard–Jones equation engaging Atom-based summation and Cubic-spline truncation method with a cut-off radius of 18.5 Å, was used to calculate the vander Waals interactions. While the long-range electrostatic interactions and Coulomb interactions were both obtained by three-dimensional Ewald Group methods, with the accuracy of 1.0e-5 kcal/mol at a cut-off distance of 18.5 Å. All the configurations considered in the analysis were converged well.

Molecular Dynamics Simulations (MD):

The 6 x 6 x 6 COF matrix embedded with the Cu frustum cluster (4 8 4, 110 basal plane) and the substrates, hexabromobenzene and 4-hydroxybenzal in the ration 1:6 were investigated using the Forcite Dynamics module embedded in the Accelrys Package. For the MD, the initial velocities were made Random. A 5 ns NVT (T = 298 K) MD simulations (1.0 fs time step) were used to reach an equilibrium state. Finally, 5 ns NPT MD simulations (1.0 fs time step) were used to generate the low-energy trajectory from which the we analyzed the radial distribution function (RDF). The Universal force field was used and the Coulumbic interactions were treated with

Ewald summation methods. Nose-Hoover Thermostat was employed to control the temperature, while Berendsen barostat helped control the pressure. Energy tolerance of 5 x 10^5 kcal/mol was applied.

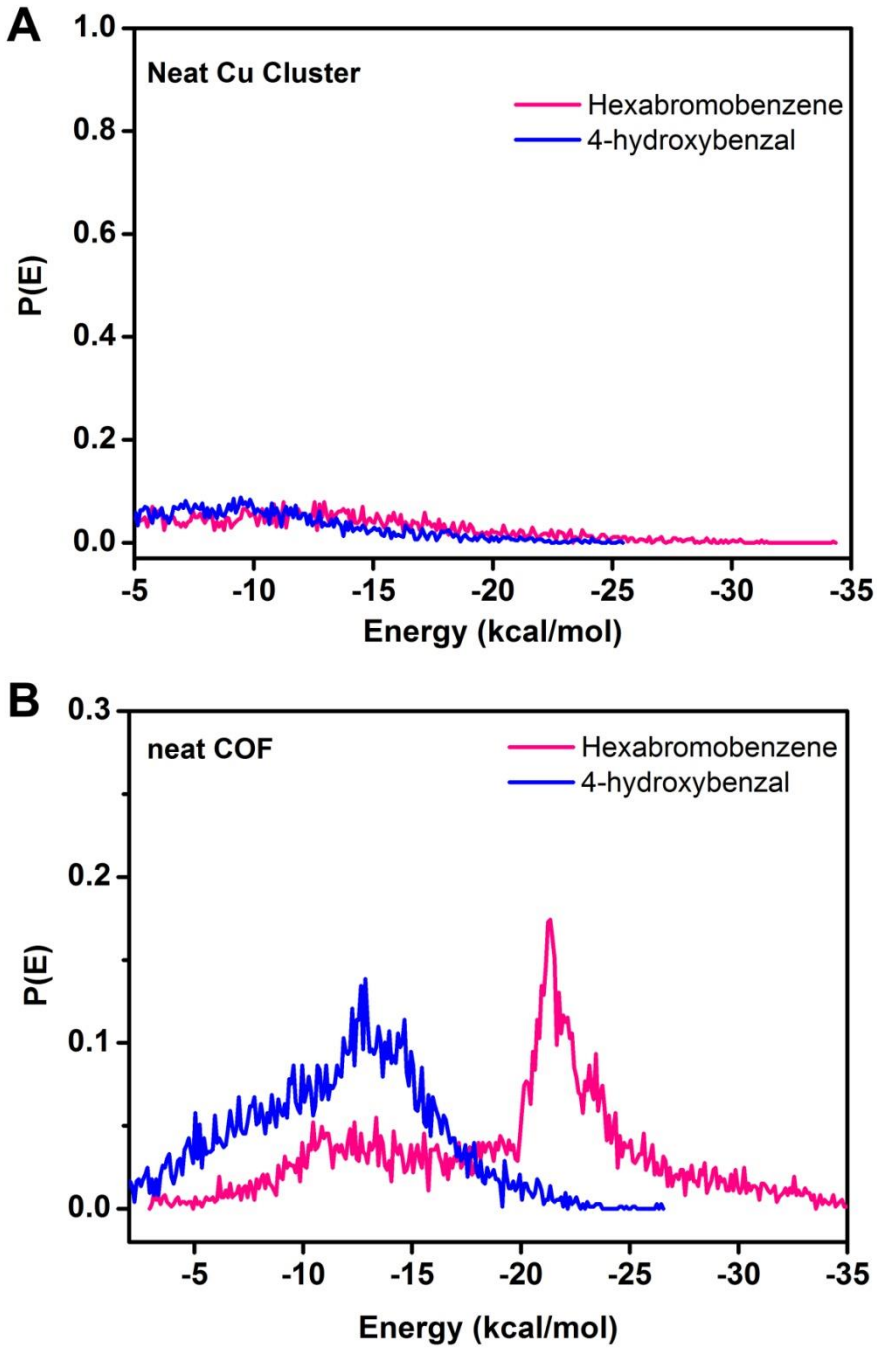

Figure S16. Adsorption energy comparisons for the substrates involved in the multi-fold coupling reactions, A: Adsorption energy probabilities for hexabromobenzene and 4-hydroxybenzal on neat isolated Cu Cluster; B: Adsorption energy probabilities for hexabromobenzene and 4-hydroxybenzal on neat IISERP-COF15. Note: These are much lower values compared to the composite (See figure 4 of the maintext).

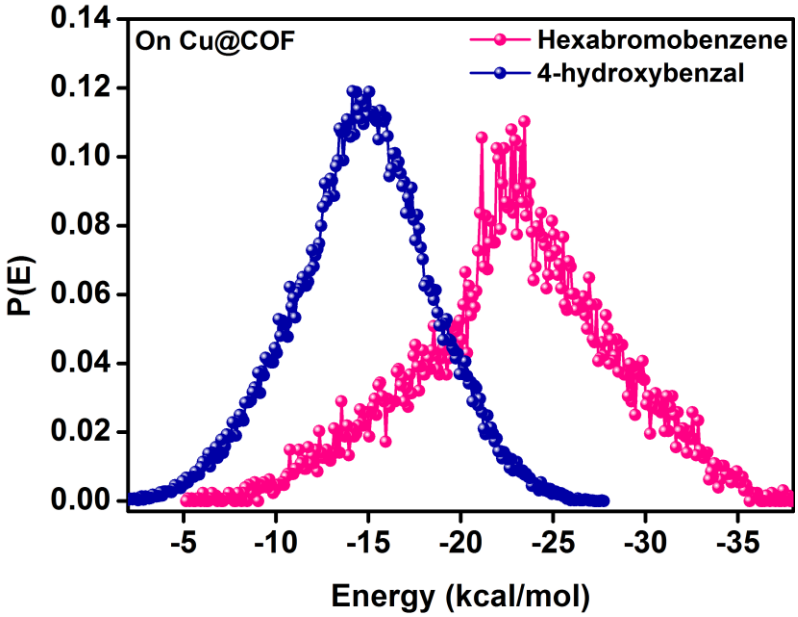

Figure S17. Adsorption energy comparisons for the substrates involved in the multi-fold coupling reactions. These are observed from the GCMC simulations carried out using models where very few copper clusters were dispersed into the COF pores to make it resemble the dilute loading conditions. Important: As expected, the energies are almost the same as observed for the relatively higher loading presented in Figure S16. However, the probabilities have lower values which is expected.

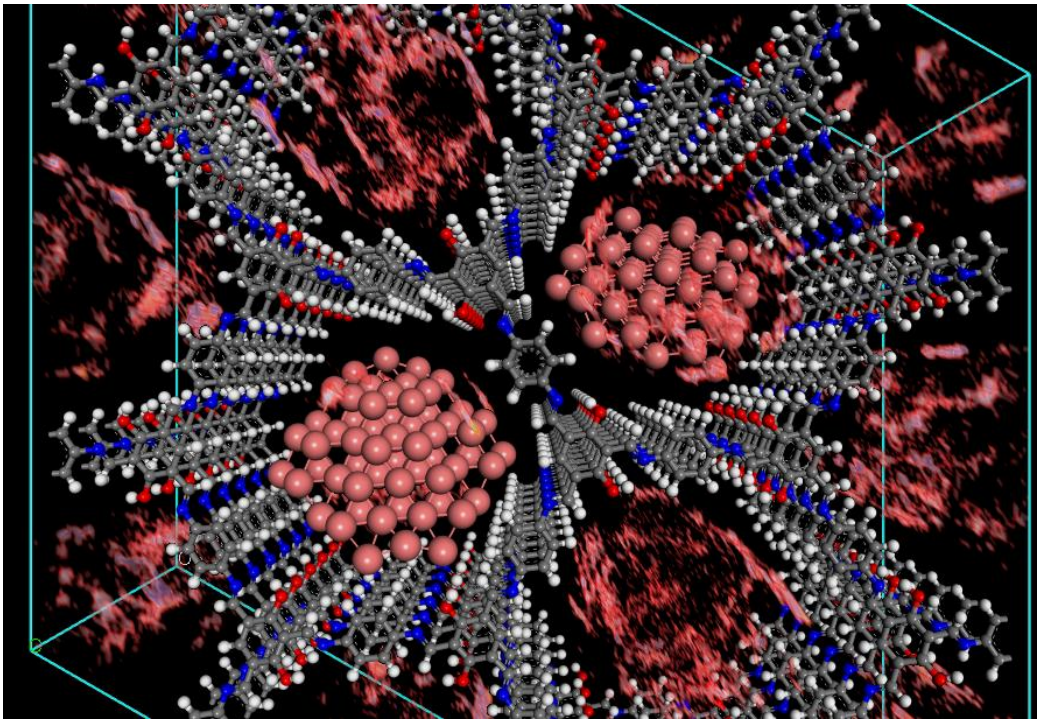

Figure S18. Optimized structure from the Simulated Annealing showing the frustum nanoclusters residing in the pore of the COF, the volume occupied by the substrates are shown as fields maps. The substrates occupy spaces above and below the cluster and confine in the nanopores.

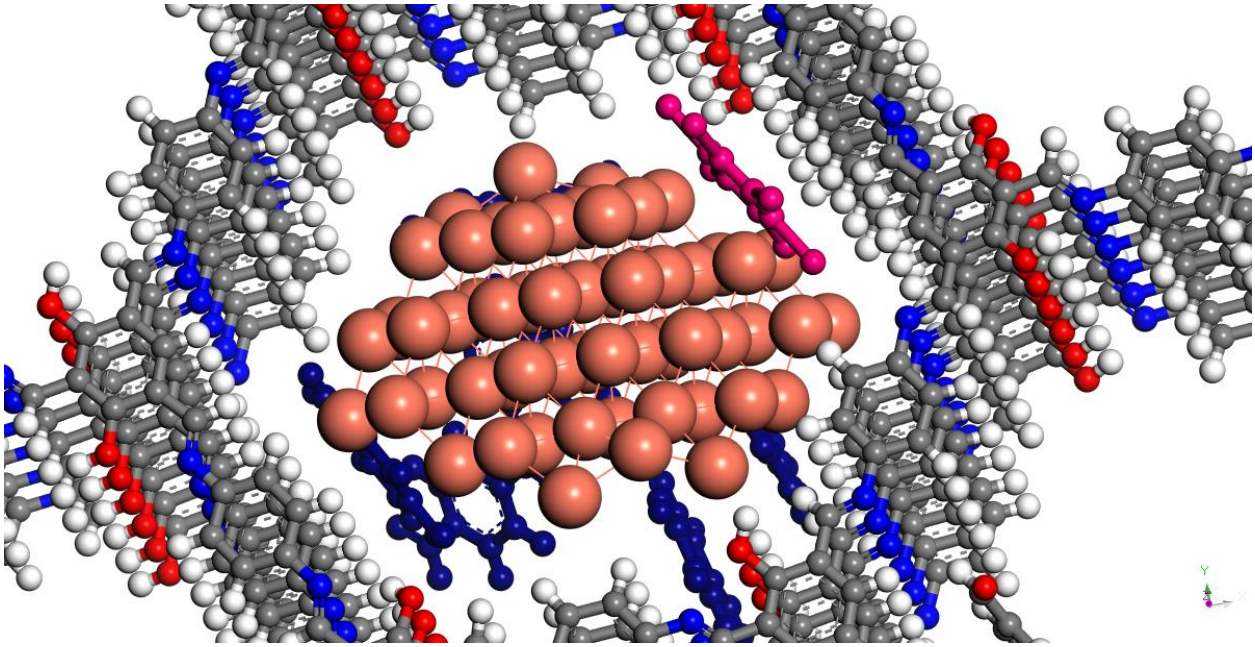

Figure S19. Selected low-energy configuration from the optimized structures. Note that the hexabromobenzene (pink) is approaching the cluster from the top, while the 4-hydroxybenzal (royal blue) substrates approach from the Cu(110) basal plane. Color code: C- grey; O- red; N- blue and H- white.

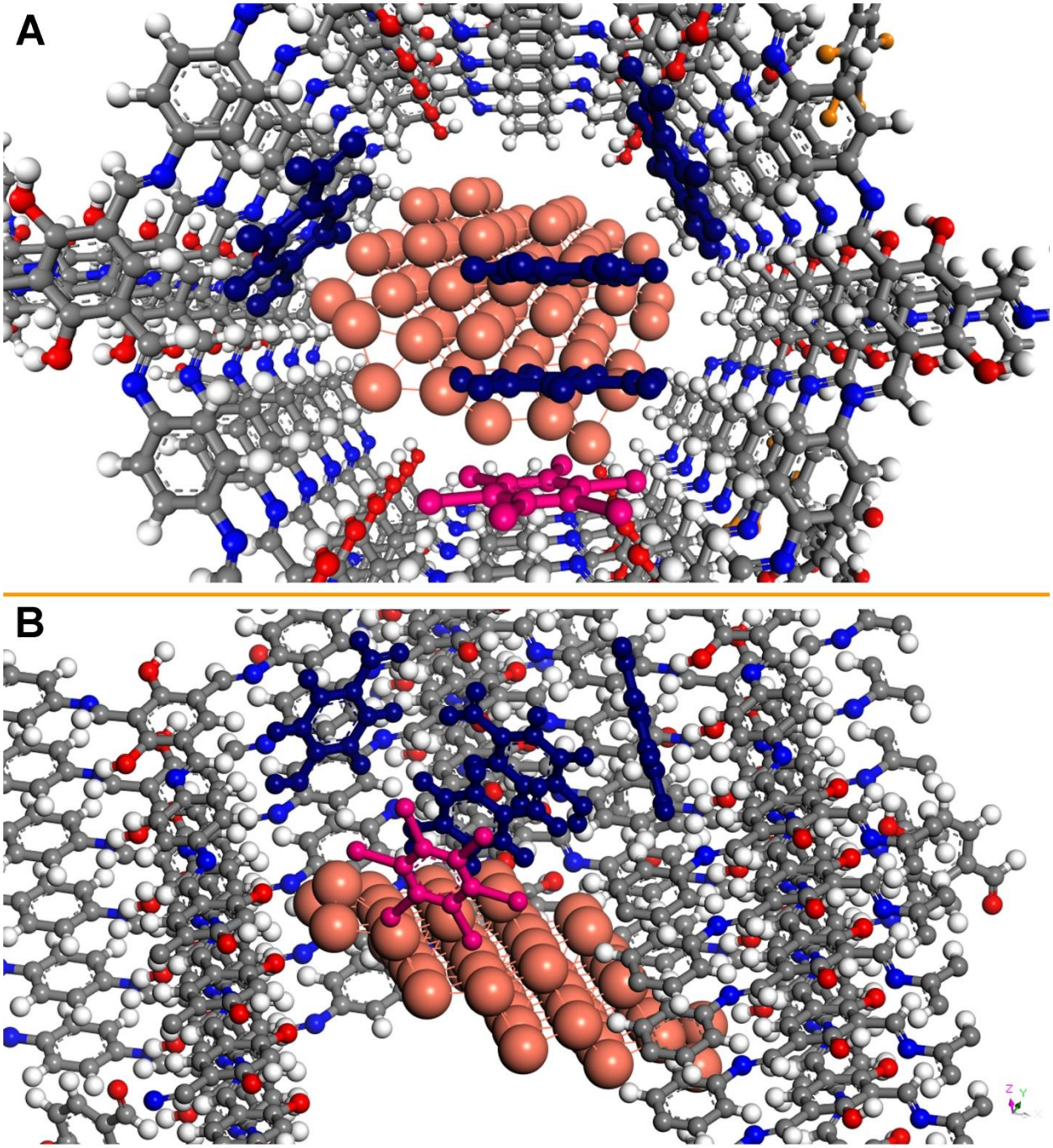

Figure S20. Another low-energy configurations from the optimized structures. Note that the 4-hydroxybenzal (royal blue) and the hexabromobenzene (pink) are approaching the Cu cluster (brown) from the top. Color code: C- grey; O- red; N- blue and H- white. Some of the atoms have been removed for clarity. Both these configurations, shown in Figure S17 and this figure have comparable energies.

Remark: A statistical distribution analysis over 1000 images reveal that the configurations shown here are representatives of frequently occurring ones and the orientations of the substrates and the cluster are almost consistent across most of the low-energy structures.

Table S1: Selected heterogeneous catalyst with Cu/Cu(I) supported on a porous material.

Ent.	Catalyst	Catalyst Loading	Yield	Time & Temp	TON	Reference
1.	CuI@MOF (CuI on Al(OH)bypdc MOF)*	20 mol% (8.26 wt% Cu)	65-96 %	36 hrs 120 °C	-	*RSC Adv*., **2012**, 2, 5528-5530
2.	CuO@MOF (CuO on UiO-66 NH_2 MOF)*	5mol% (7.2 wt% Cu)	30-95%	18-24 hrs 110°C	-	*New J. Chem*., **2017**, 41, 12014-12027
3.	Cu(0)NPs@POF*	3 mol% (7.3 wt% Cu)	90-100%	24 hrs 110°C	-	*Molecular Catalysis*, **2021**, 504, 111460
4.	Mesoporous Cu(II)O/MnO*	3 mol %	26-95%	20 hrs 140°C	22-33	*Inorg. Chem*., **2017**, 56, 10290−10297
5.	Cu(0)@MCTP (Covalent Triazine polymer)*	100 mg (2.68 wt% Cu) Size=3nm	77 -97%	24 hrs 130°C	-	*Catal. Sci. Technol*., **2016**, 6, 1701–1709
6.	Cu(0)NPs/CNFs (C Nanofiber supported CuNPs)	90 mg (7.07 wt% Cu)	80-100%	24 hrs 140°C	-	*RSC Adv*., **2014**, 4, 48362–48367
7.	Porous PDVB-SB-Cu(I) (Schiff base Polydivinyl benzene-Cu)*	20 mol%	80-99 %	16 hrs 115°C	-	*ChemCatChem*, **2013**, 5, 1606 – 1613
8.	Polystyrene Polymer/Cu(II)	9.8 mol% (3.36 wt% Cu)	56-95 %	14 hrs 120°C	-	*J. Organomet. Chem*., **2012**, 696, 4264–4274
9.	Cu(0)NPs/Electrospundoped CNFs	100 mg	47-100 %	24 hrs 140°C	-	*Catal. Lett*., **2015**, 145, 1764–1770
10.	Cu(0)@COF	0.25 mol% (3.34 wt%)	80-100 %	24 hrs 135°C	320-392	**This work**

Note: * represents system with Cu or Cu(II) supported on porous materials. Among all the systems reported above, the current system Cu@COF has the best TON due to low catalyst loading and the high yield is obtained under comparable conditions. This proves the advantage the crystalline structure with ordered pores could bring.

References:

S1. S.Halder, D. Chakraborty, B. Roy, G. B. Banappanavar, R. Kushwaha, D. Mullangi, P. Hazra, D. Kabra and R. Vaidhyanathan, *J. Am. Chem. Soc*., 2018, **140**, 13367−13374.
S2. D. Chakraborty, P. Shekhar, H. D. Singh, R. Kushwaha, C. P. Vinod and R.Vaidhyanathan, *Chem.Asian J*., 2019, **14**, 4767 –4773 .
S3. V. Cerny, *J. Optim. Theor. Appl.*, 1985, **45**, 41-51.
S4. D. Frenkel, B. Smit, Understanding Molecular Simulation: From Algorithms to Applications, 2nd Edition, Academic Press: San Diego (2002).
S5.S. Kirkpatrick, C. D. Gelatt and M. P. Vecchi, *Science, 1983, **220**,* 671-680.
S6. R. F. Hout, W. J Pietro and W. J. Hehre, " *J. Comput. Chem.*, 1983, **4**, 276.

7. Appendix

Nuclear Magnetic Resonance (NMR), High Resolution Mass Spectroscopy (HRMS) data:

1. Phenoxybenzene

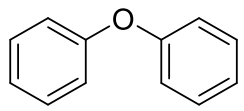

^{1}H NMR (400 MHz, DMSO): δ= 7.38 – 7.29 (m, 4H), 7.11 (t, 2H), 7.02 (m, 4H).

^{13}C NMR (101 MHz, DMSO): δ =156.87 (s), 130.26 (s), 123.65 (s), 118.82 (s).

HRMS: calcd 170.07, found 170.09

2. 4-Phenoxybenzaldehyde

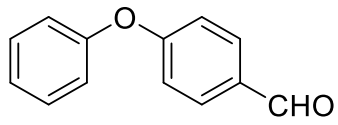

^{1}H NMR (400 MHz, $CDCl_3$): δ= 9.95 (s, 1H), 7.91 – 7.83 (d, 2H), 7.48 – 7.41 (t, 2H), 7.28 – 7.22 (m, 1H), 7.15 – 7.06 (m, 4H) .

^{13}C NMR (101 MHz, $CDCl_3$) δ =191.27 (s), 163.70 (s), 155.53 (s), 132.41 (s), 130.60 (s), 125.40 (s), 120.88 (s), 118.01 (s) .

HRMS: calcd 198.07, found 199.07

3. 1,3-Dimethyl-5-phenoxybenzene

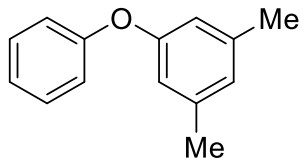

^{1}H NMR (400 MHz, $CDCl_3$): δ= 7.38 – 7.31 (dd, 2H), 7.26 (t, 1H), 7.14 – 7.07 (d, 2H), 7.04 – 7.00 (s, 1H), 6.77 (s, J = 0.8 Hz, 1H), 6.66 (s, 1H), 2.33 (s,6H).

^{13}C NMR (101 MHz, $CDCl_3$) δ = 157.55 (s), 157.27 (s), 139.70 (s), 129.77 (s), 125.11 (s), 123.10 (s), 118.97 (s), 116.72 (s), 21.44 (s).

HRMS: calcd 198.10, found 198.10

4. 1-Nitro-4-phenoxybenzene

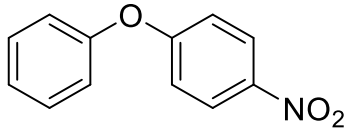

^{1}H NMR (400 MHz, DMSO): δ 8.26 – 8.21 (m, 2H), 7.51 – 7.45 (m, 2H), 7.32 – 7.26 (m, 1H), 7.19 – 7.15 (m, 2H), 7.13 – 7.08 (m, 2H).

^{13}C NMR (101 MHz, $CDCl_3$): δ= 164.26 (s), 155.56 (s), 131.20 (s), 126.82 (s), 126.30 (s), 121.43 (s), 117.95 (s).

HRMS: calcd 215.06, found 216.08

5. 3-Phenoxybenzonitrile

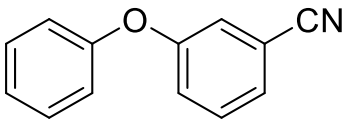

^{1}H NMR (400 MHz, $CDCl_3$): δ =7.45 – 7.32 (m, 2H), 7.25 – 7.17 (m, 3H), 7.08 – 7.00 (m, 4H).

^{13}C NMR (101 MHz, $CDCl_3$): δ= 158.30 (s), 155.63 (s), 130.78 (s), 130.31 (s), 126.52 (s), 124.84 (s), 122.88 (s), 121.18 (s), 119.90 (s), 118.40 (s), 113.65 (s).

HRMS: calcd 195.07, found 196.07

6. 1-methoxy-4-phenoxybenzene

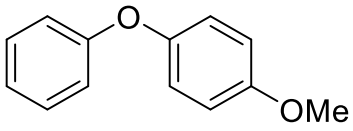

^{1}H NMR (400 MHz, $CDCl_3$): δ= 7.33 – 7.27 (m, 2H), 7.08 – 7.01 (m, 1H), 7.01 – 6.93 (m, 4H), 6.91 – 6.86 (m, 2H), 3.90 – 3.70 (m, 3H).

^{13}C NMR (101 MHz, $CDCl_3$): δ= 158.97 (s), 156.35 (s), 150.58 (s), 130.06 (s), 122.88 (s), 121.29 (s), 118.04 (s), 115.31 (s), 56.11 (s).

HRMS: calcd 200.08, found 201.07

7. 4,4’,4”,4,’’’,4””,4’’’’’-(benzene -1,2,3,4,5,6 hexaylhexakis(oxy) hexabenzaldehyde

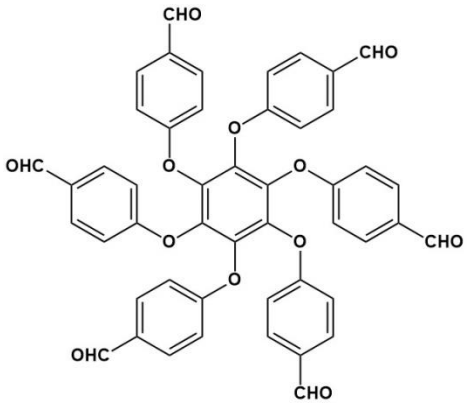

1H NMR (400 MHz, DMSO): δ= 9.95 (s, 6H), 8.00 – 7.95 (m, 12H), 7.28 – 7.24 (m, 12H).

13C NMR (101 MHz, DMSO): δ= 191.95 (s), 160.66 (s), 132.35 (s), 119.61 (s), 115.83 (s).

HRMS: calcd 798.17, found 798.86

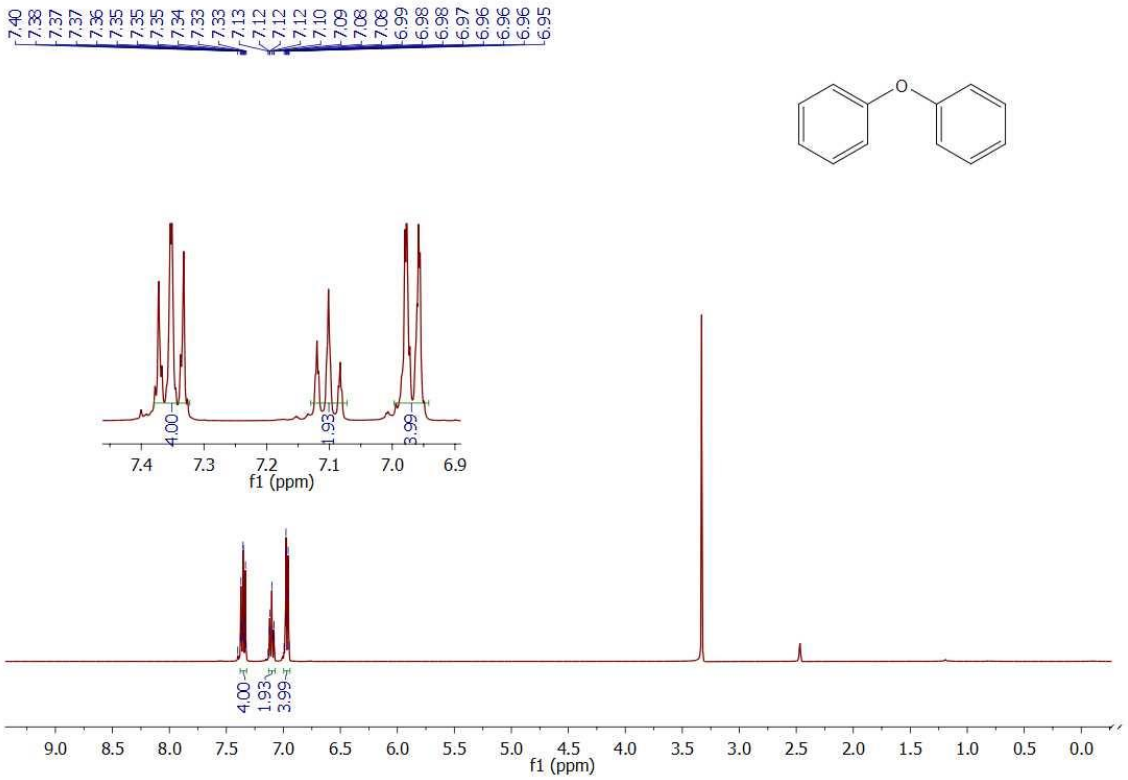

Figure S21. ^{1}H NMR of phenoxybenzene showing characteristic peaks and no. of protons.

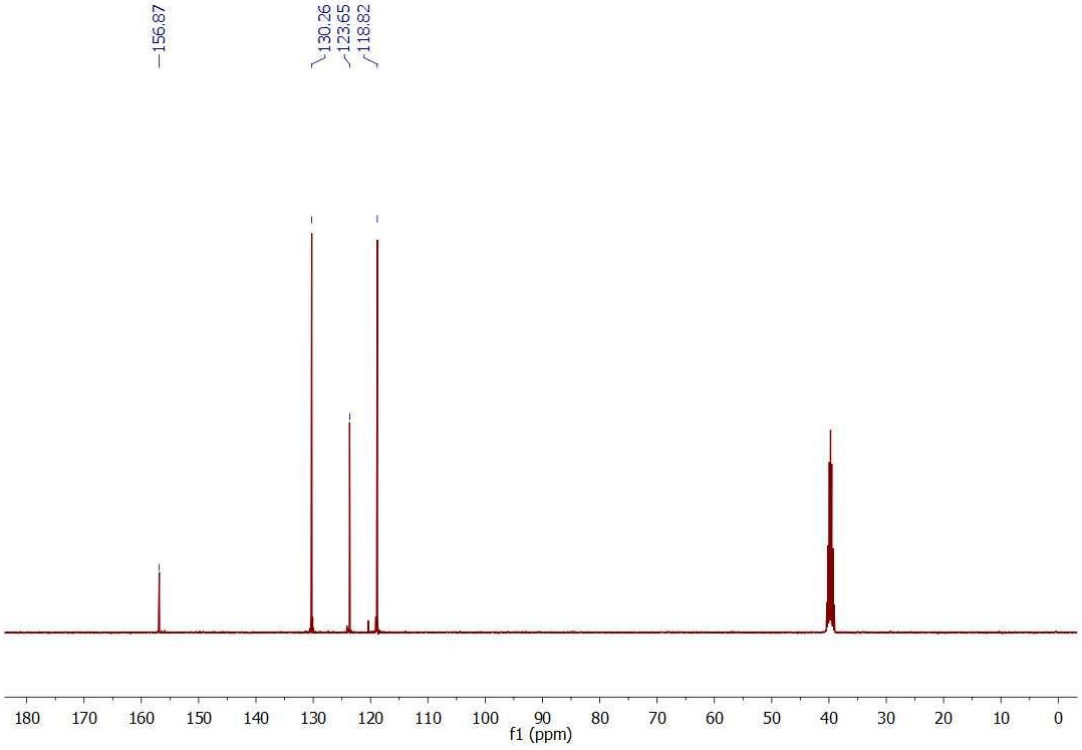

Figure S22. ^{13}C NMR of phenoxybenzene showing all the characteristic peaks.

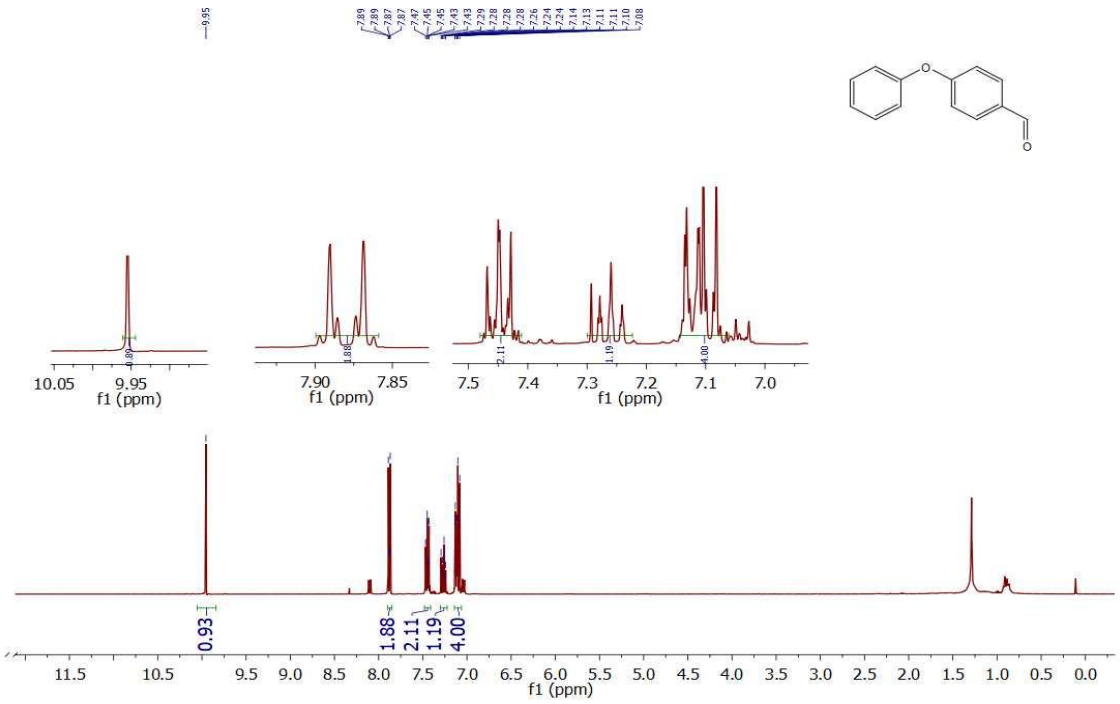

Figure S23. [1]H NMR of ,4-hydroxybenzaldehyde showing characteristic peaks and no. of protons.

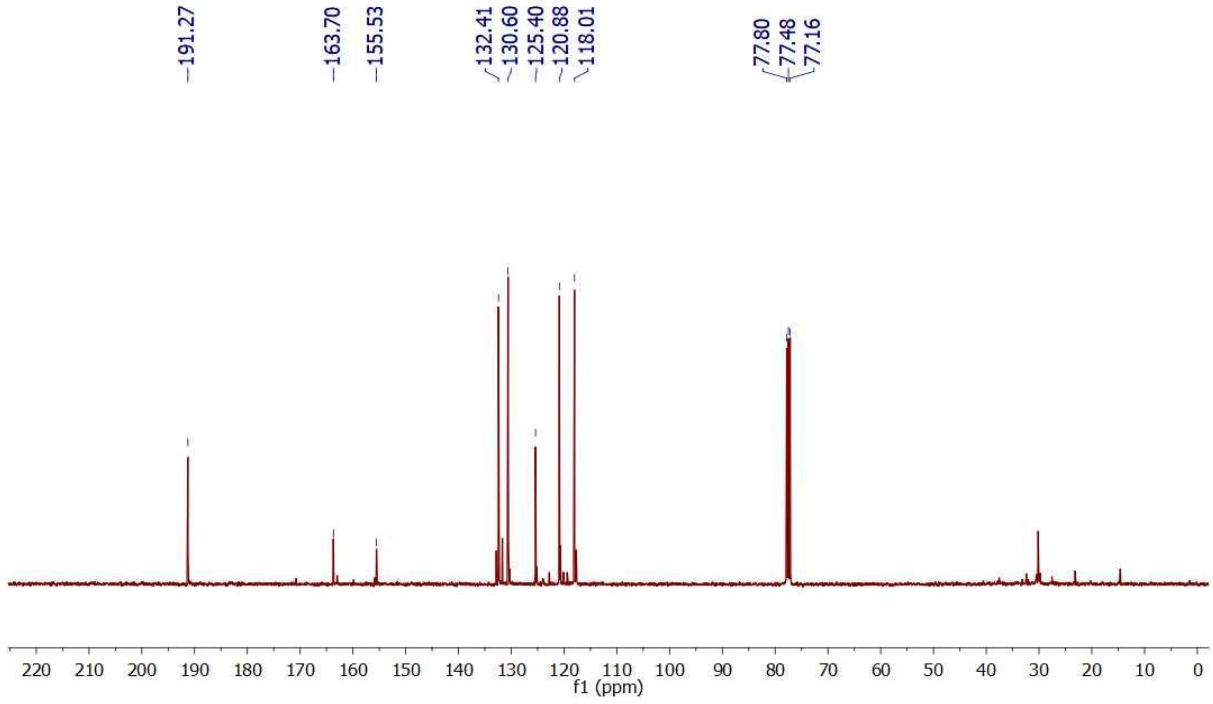

Figure S24. [13]C NMR of 4-hydroxybenzaldehyde showing all the characteristic peaks.

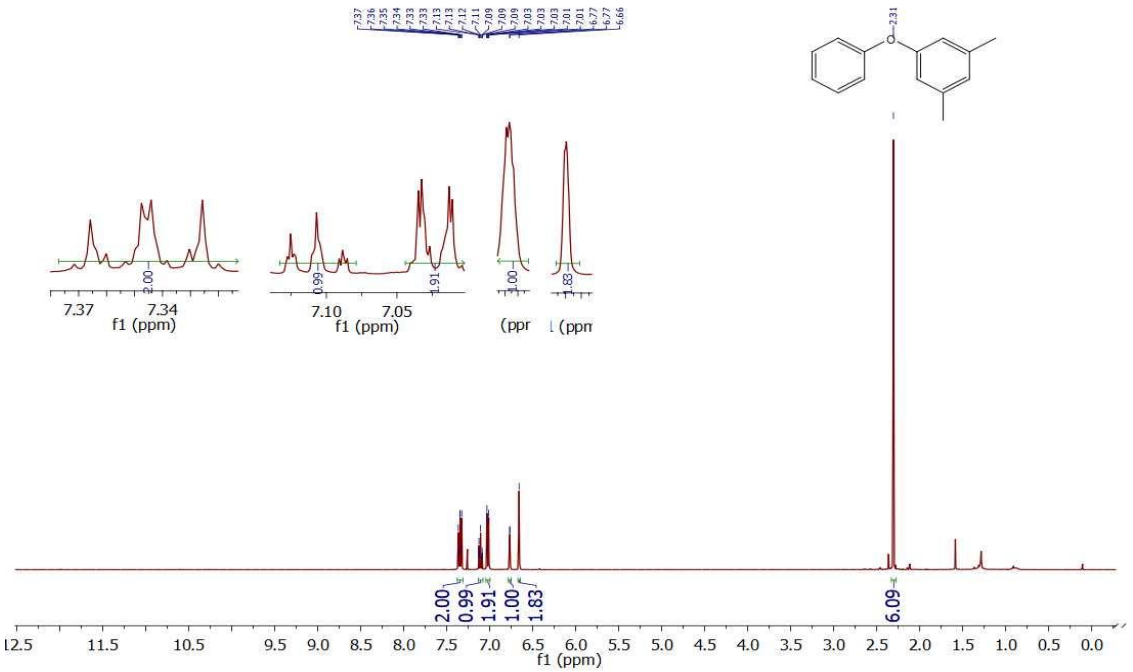

Figure S25. [1]H NMR of 1,3-dimethyl-5-phenoxybenzene showing characteristic peak and no. of protons.

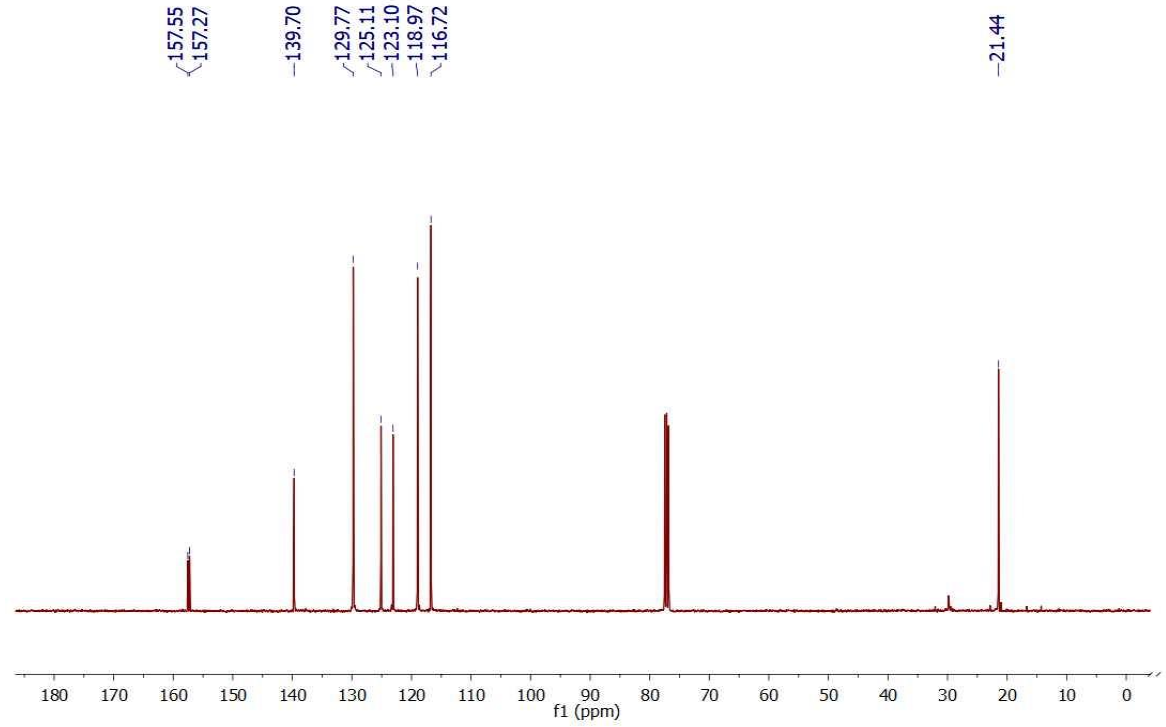

Figure S26. [13]C NMR of 1,3-dimethyl-5-phenoxybenzene showing all the characteristic peaks.

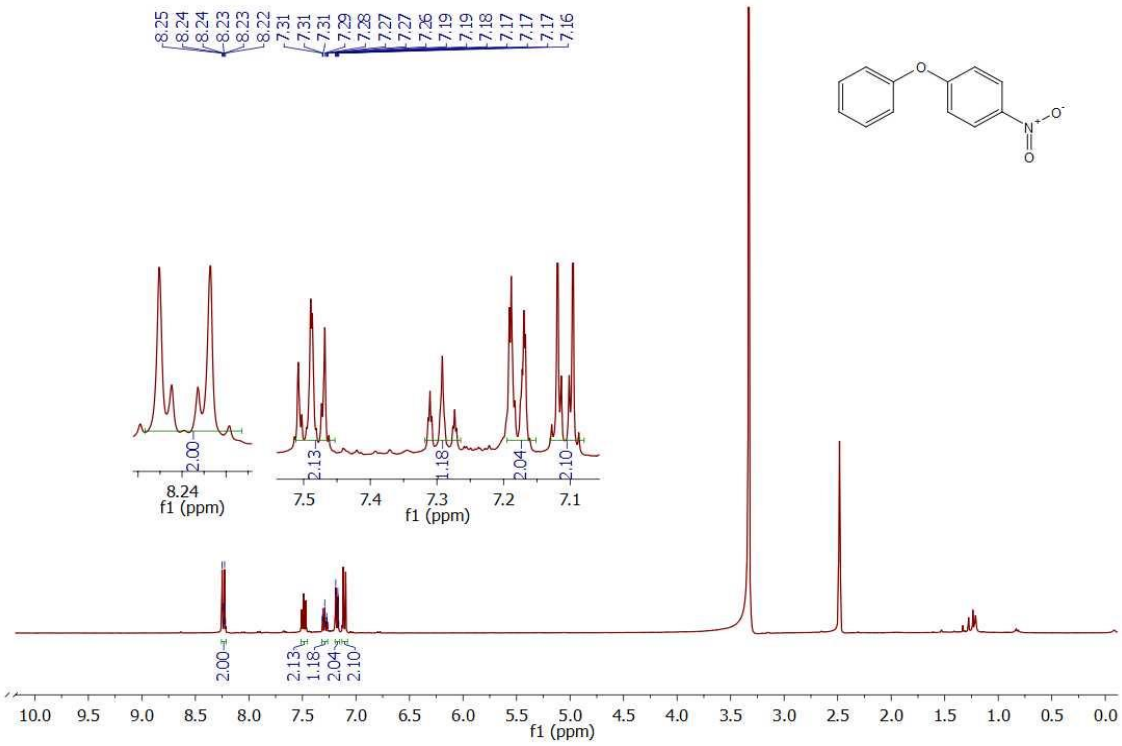

Figure S27. [1]H NMR of 1-nitro-4-phenoxybenzene showing characteristic peaks and no. of protons.

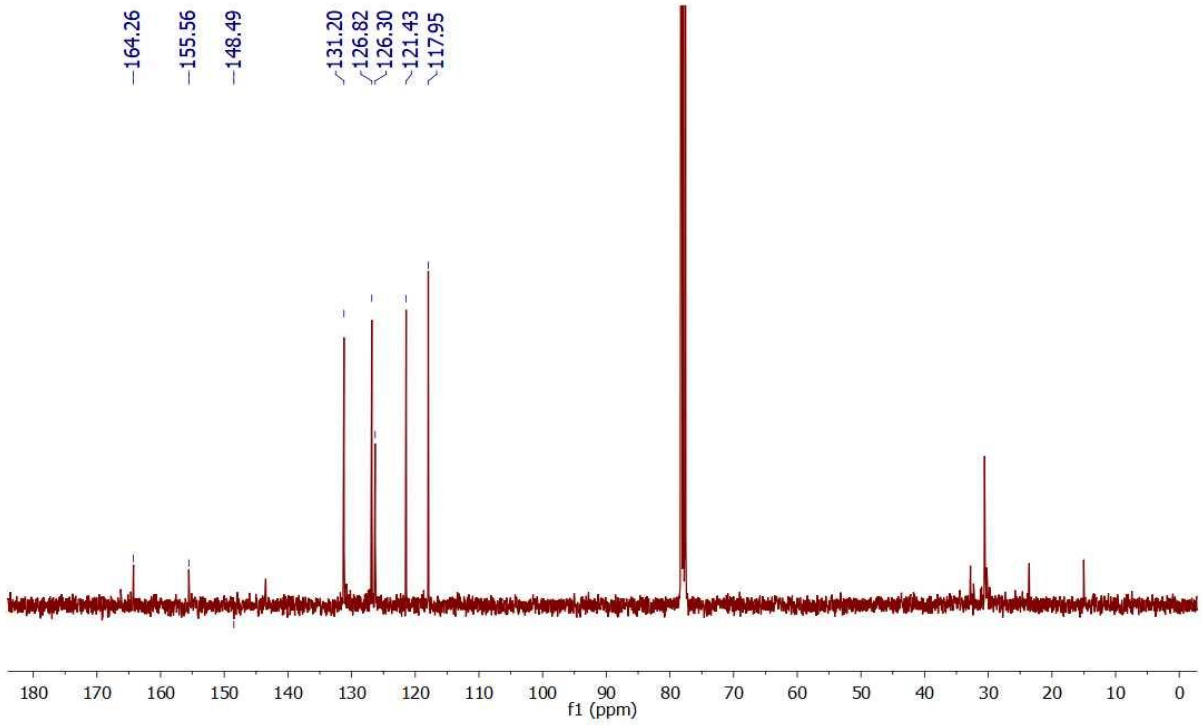

Figure S28. [13]C NMR of 1-nitro-4-phenoxybenzene showing all the characteristic peaks.

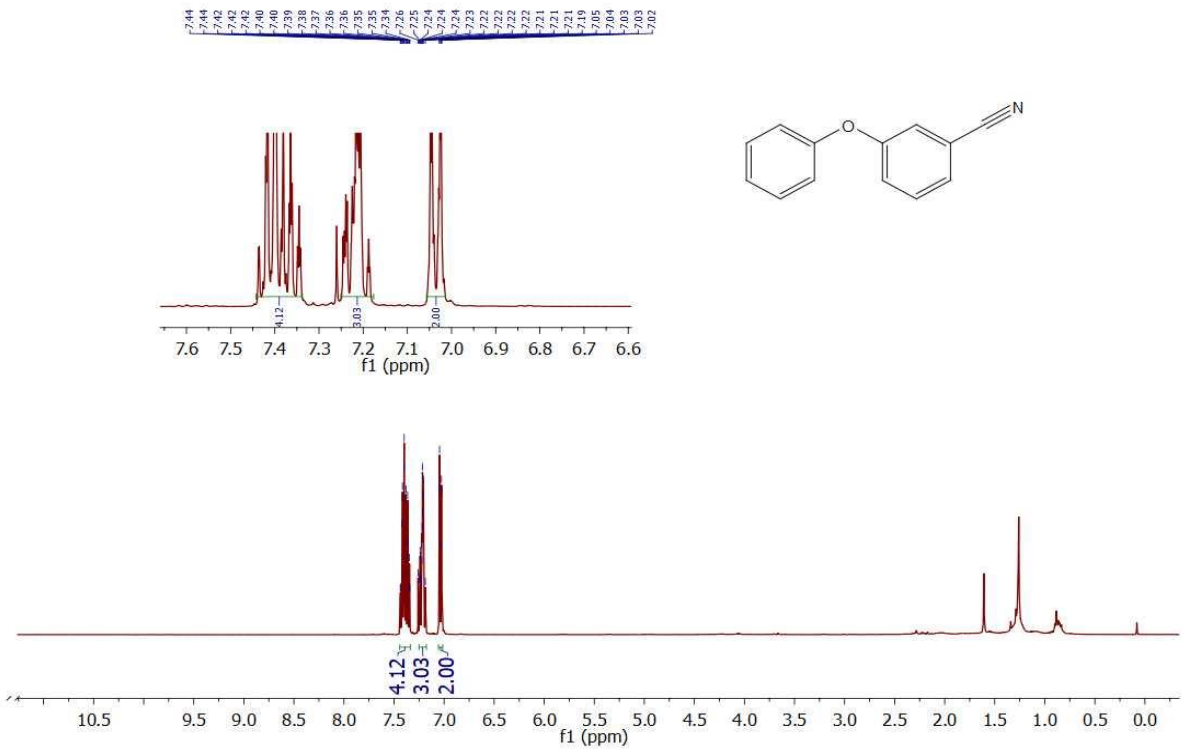

Figure S29. ^{1}H NMR of 3-phenoxybenzonitrile showing characteristic peaks and no. of protons.

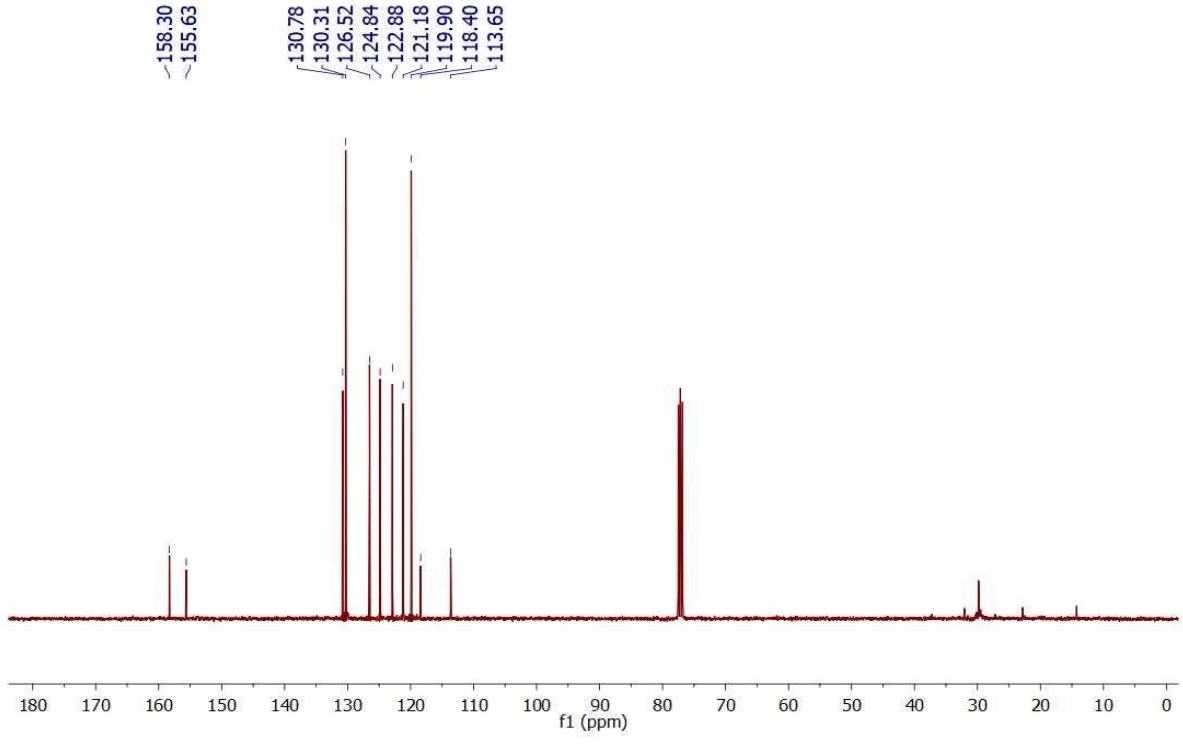

Figure S30. ^{13}C NMR of 3-phenoxybenzonitrile showing all the characteristic peaks.

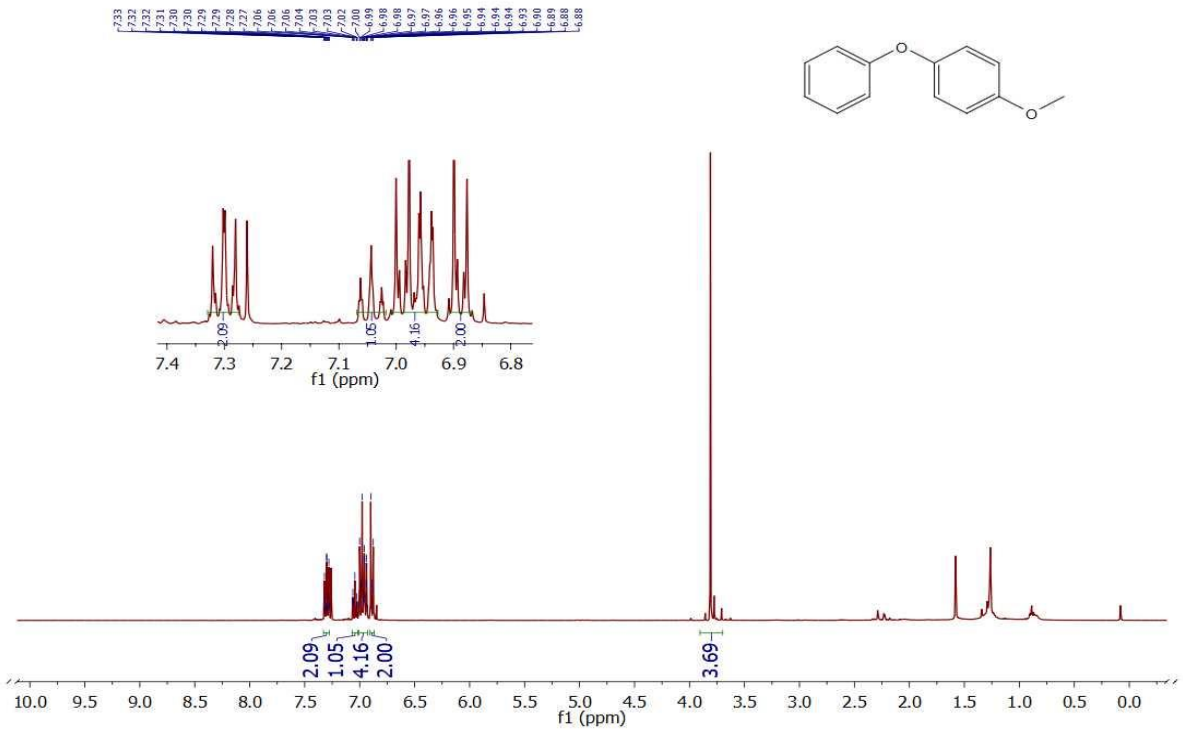

Figure S31. ^{1}H NMR of 1-methoxy-4-phenoxybenzene showing characteristic peaks and no. of protons.

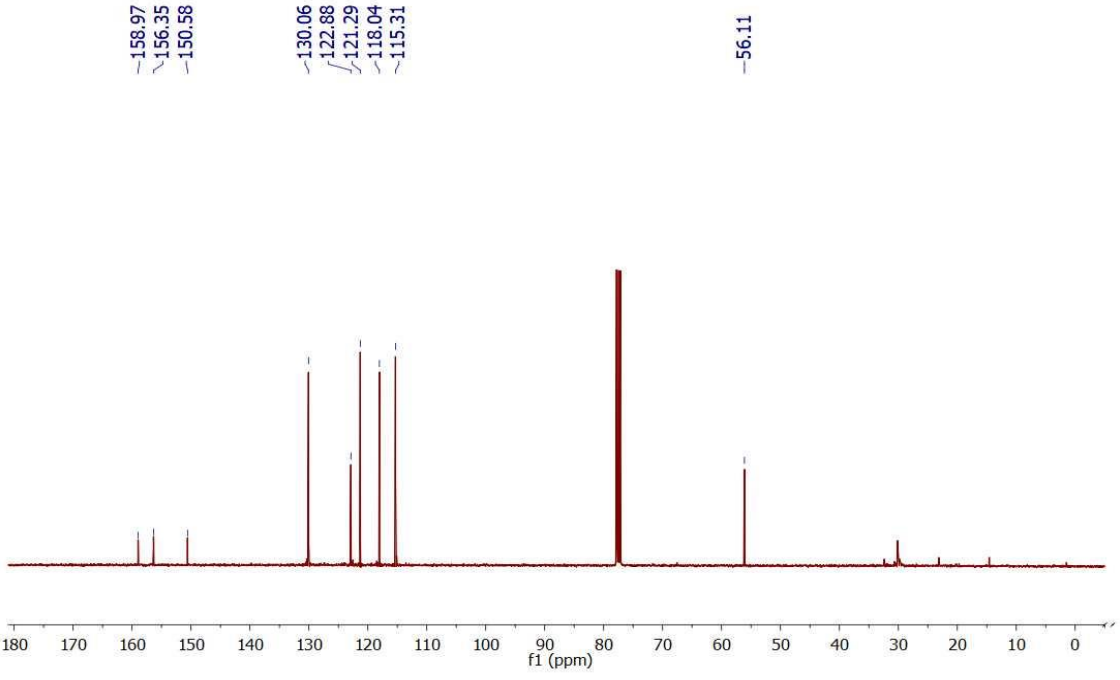

Figure S32. ^{13}C NMR of 1-methoxy-4-phenoxybenzene showing all the characteristic peaks.

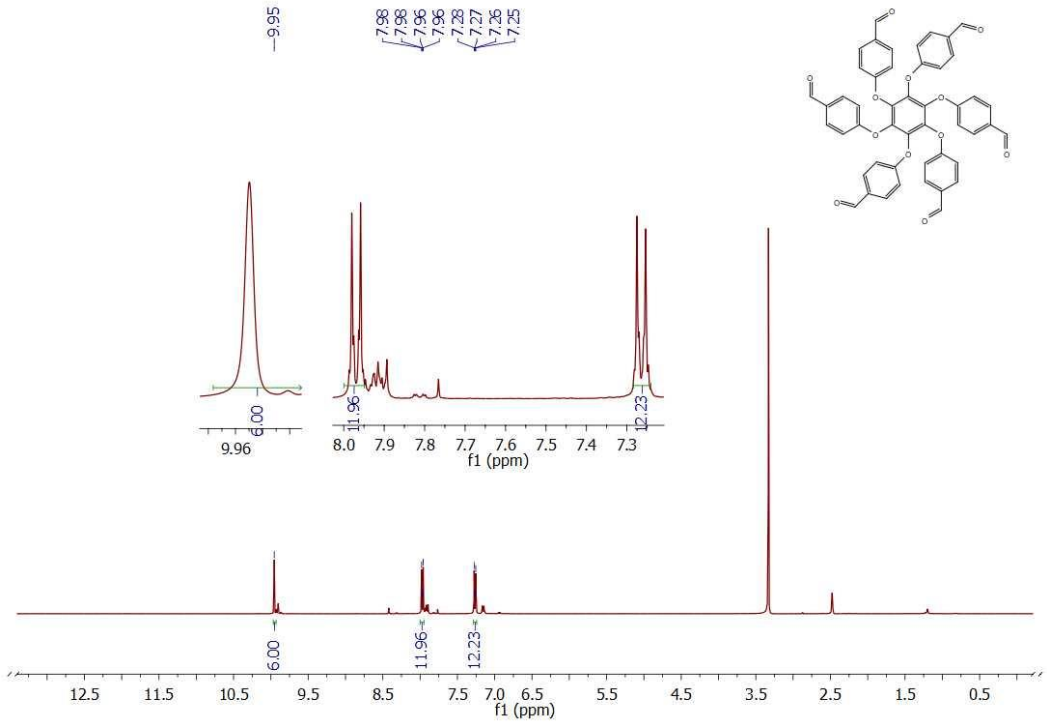

Figure S33. ^{1}H NMR of 4,4',4",4,''',4"",4'''''-(benzene -1,2,3,4,5,6 hexaylhexakis(oxy) hexabenzaldehyde showing characteristic peaks and no. of protons.

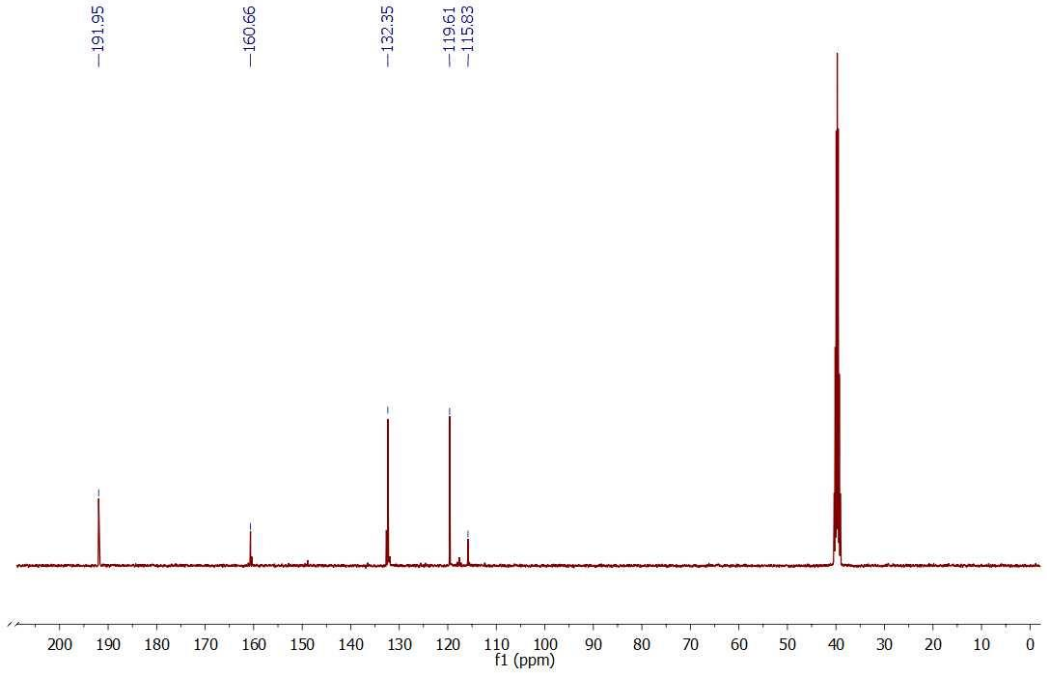

Figure S34. ^{13}C NMR of 4,4',4",4,''',4"",4'''''-(benzene -1,2,3,4,5,6 hexaylhexakis(oxy) hexabenzaldehyde showing characteristic peaks.